Journal of Constructional Steel Research 190 (2022) 107117

Contents lists available at ScienceDirect

Journal of Constructional Steel Research

journal homepage: www.elsevier.com/locate/jcsr

# Post-buckling shear resistance of slender girder webs: Stiffener participation and flange contributions

Kevin E. Augustyn [a], Spencer E. Quiel [a,*], Maria E.M. Garlock [b]

[a] Department of Civil and Environmental Engineering, Lehigh University, Bethlehem, PA, USA
[b] Department of Civil and Environmental Engineering, Princeton University, Princeton, NJ, USA

ARTICLE INFO

Keywords:
Web shear buckling
Slender steel plate girder
Initial web imperfections
Ultimate shear resistance

ABSTRACT

A series of validated finite element models are used to parametrically evaluate the participation of flanges and transverse stiffeners in the post-buckling web shear mechanics of welded I-shaped steel plate girders. The models are validated against the results of six large-scale web shear-buckling tests from the existing literature on highly slender plate girders (with web slenderness ratios of 250–267) and varying transverse stiffener spacing (with web panel aspect ratios from 1 to 4). All girders exhibited a 3-stage web shear-buckling response: 1) an initial linear elastic stage, 2) a post-buckling stage I during which shear stiffness begins to progressively decrease, and 3) a post-buckling stage II with either significantly reduced or negative stiffness after the buckled web panel has formed a yield mechanism. Increasing the flange thickness in a given girder configuration can change the mode of the post-buckling stage II response from gradual unloading (with ultimate shear reached at the end of post-buckling stage I) to positive hardening (with ultimate shear instead reached during post-buckling stage II at much larger displacement and with a 5–15% increase in shear resistance from the end of post-buckling stage I). At ultimate shear, the transverse stiffeners develop axial forces that equal only 10–30% of the applied shear load depending on their sizing, the panel aspect ratio, and the web plate thickness. The stiffeners are primarily engaged in the web's out-of-plane direction to impose panelization and less as an axial strut for the post-buckling load path.

## 1. Introduction

Deep I-beams fabricated from welded flat steel plates (e.g., plate girders) have been commonly used in steel construction practice worldwide for more than a century. To maximize their material efficiency, plate girder design relies heavily on the shear capacity of the slender web, thus maximizing flange separation and minimizing self-weight to meet the flexural demands of long spans. Web plates that elastically buckle due to shear still possess a significant amount of post-buckling shear resistance [1], which is considered in contemporary strength-based design of slender steel plate girders [2–4]. Over the last century, more than a dozen proposals have been developed to explain and predict the post-buckling shear strength of thin webs in plate girders based on tension field action [5], which posits that the main source of post-buckling shear strength is the development of tensile stresses in a defined diagonal field that is mobilized after elastic shear buckling [6]. The dimensions of these diagonal tension fields are defined by the intermittent placement of vertical (e.g., transverse) stiffeners, which are typically welded to the web to create panel zones with a targeted aspect ratio.

The evolution of the various proposed models for post-buckling behavior in slender web plates (including the supporting experimental and computational literature) has been extensively documented in two recent journal publications [7,8]. With a few exceptions [9], nearly every model incorporates some form of tension field action [5]. The primary differences between the various models focus on the assumed shape of the tension diagonal in the stiffened web panel and the distribution of the shear stresses in the web to the bordering stiffeners and flange plates after buckling occurs. The earliest attempts at deciphering the mechanics of web shear post-buckling in the 1890's [10–14] suggested that a buckled web panel (defined by intermediate vertical stiffener placement) would emulate a Pratt or N-type truss. Per this theory, the tension diagonal that develops across the buckled web would be anchored at its ends to the flange (acting as a horizontal chord) and/or an intermediate stiffener (acting as a vertical truss element that transfers load between the chords). About 50 years later, researchers at

* Corresponding author.
E-mail address: squiel@lehigh.edu (S.E. Quiel).

https://doi.org/10.1016/j.jcsr.2021.107117
Received 13 October 2021; Received in revised form 16 December 2021; Accepted 21 December 2021

Lehigh University further investigated the role of tension field action in the post-buckling ultimate capacity of slender plate girder webs. Via a series of tests in the late 1950's, Basler et al. [15–17] proposed the foundational model for tension field action which still serves as the basis for many modern design standards.

Since then, numerous studies have proposed modified theories and mechanical models of web shear buckling behavior [7]; a summary of the most prominent among these models is presented in Section 2. Despite the ongoing research exploration of the web shear buckling mechanism, disagreements persist regarding, among other things, (1) the role of the stiffeners and flanges in anchoring the tension field, (2) the contribution of compression forces that emerge in the buckled web in the direction orthogonal to the tension field, and (3) the width of the tension field itself. Convincing methods are needed to examine the load flow within the web panel as well as between the web, flange, and stiffener plates during the post-buckling stages of web shear behavior.

In this paper, the two seminal girder tests at Lehigh University by Basler et al. (specimens G6 and G7 [15–17]) as well as four recent tests at the Technical University of Denmark by Hansen (specimens G1 through G4 [18,19]) are used as the basis for numerical investigation, first for finite element (FE) model validation and then for parametric evaluation. The participation of the flanges and stiffeners in anchoring the tension field in the buckled web as well as their contributions to the load path at ultimate shear resistance are evaluated via systematic sizing variation. The modeling results are used to illustrate the sensitivity of the shear post-buckling response, particularly the onset of subsequent post-yield behavior, to the relative stiffnesses of the web, flange, and stiffener plates. Furthermore, the results compared with the presumed levels of flange and stiffener participation that are inherent in current design models for tension field action in buckled slender webs under shear.

## 2. Background

As shown in Fig. 1a, a flat web plate loaded in pure shear will theoretically have principal stresses acting at a 45° angle prior to elastic buckling. In Fig. 1b, Basler's model [15] suggests that the diagonal tension in the pre-buckled web intensifies after the web has buckled, thus forming a discrete tension field at an angle that is now shallower than 45°. Basler's model relies on several assumptions regarding the load path in the buckled web once the tension field has developed. By providing out-of-plane flexural stiffness, the intermediate stiffeners define the panelization that enables the emergence of the diagonal tension field after buckling occurs. By assuming that the buckled web loses most of its compressive resistance in the direction orthogonal to the tension field, Basler stated that "the stiffener must take the vertical component of the diagonal stresses out of the web at one end and transfer them to its other end" as a compression strut between the chords [15]. The flanges then "exhibit a tendency toward truss action" [17] to resolve the loads as chords that anchor the vertical stiffeners. Basler assumed that the flange plates lacked the weak axis flexural stiffness that would be needed to directly anchor the tension forces in the web diagonal – this is expressed in Fig. 1b, in which the ends of the tension field are anchored to the stiffeners and then terminate at the stiffener-to-flange interface. Subsequent experimental [20] and computational [21] studies by Lee and Yoo also indicated that direct anchorage of the tension field to the flange was not necessary to mobilize post-buckling tension field action. Also, a recent computational study by Alinia et al. [22] suggested that the locations of post-buckling flange deformation are not directly correlated to the anchorage of the tension field stresses but rather a byproduct of the increasingly large shear deformations of the buckled panel.

Despite the widespread use of Basler's model in current practice, the role of the intermediate vertical stiffener in the model's load path has come into question in recent decades. During that time, several studies [23–28] have shown that the transverse stiffeners develop much less compression than would be expected in a Pratt truss emulation. Instead, these plates would primarily experience bending and provide out-of-plane stiffening to define the web panelization. As a result, the AASHTO [2] and AISC [3] design requirements for steel plate girders as of 2010 no longer stipulate axial resistance requirements for the intermediate vertical stiffeners. Instead, the commentary in these standards now suggests that the web itself provides the vertical compression strut to emulate the Pratt truss load path.

Additional studies have gone further to suggest that the vertical compression strut via either the stiffener or the web plays a smaller role than Basler's original model suggested. For example, research by Yoo and Lee [29] suggested that the web, with sufficiently stiff boundary conditions, could self-equilibrate using the increase of compression stresses at the corners of the compression diagonal. Recent work by Glassman and Garlock [9] showed that the buckled web still retains some of its compressive resistance in the direction orthogonal to the tension field. Localized second-order bending in the buckled web due to the progression of out-of-plane deformations can also contribute to the ultimate shear post-buckling capacity, as demonstrated by Garlock et al. in a recent computational study [30].

The Basler model's discounting of flange anchorage at the ends of the tension field has also been challenged by subsequent research studies. Experimental tests in the mid-1960's at Cardiff University [31,32] indicated that the flanges for some plate girders can be engaged in localized flexure to contribute to the post-buckling resistance of slender webs. As shown in Fig. 1c, the resulting Cardiff model posits that the tension field is anchored to both the stiffener and the flange, and the ultimate post-buckling capacity is influenced by the development of plastic hinges at the flange-to-stiffener interface as well as in the flange at the edge of the tension field width [33]. Höglund [34] subsequently proposed a model based on "rotated stress field" theory – once shear buckling occurred in unstiffened girders, the resulting web membrane stresses would need to be anchored to "rigid" end posts to fully develop the shear resistance. The initial formulation of this model neglected the influence of the flanges on the post-buckling behavior; however, subsequent iterations would be expanded to include stiffened girders where

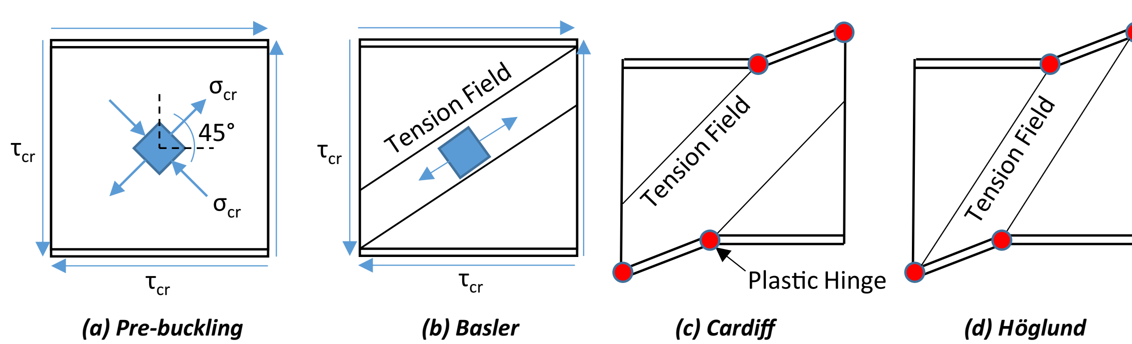


**Fig. 1.** Prominent tension field theories for stiffened slender webs in plate girders under pure shear.

the tension field would span flange-to-flange and eventually create a plastic mechanism as shown in Fig. 1d. Höglund's rotated stress theory currently serves as the basis for web shear post-buckling calculations in Section 5 of Eurocode 3, Part 1–5 [4] as well as in Section G.2.1 of AISC 360–16 for calculating shear strength of webs without tension field action [3].

In 2008, White and Barker [5] used 12 previously proposed iterations of these post-buckling models to predict the ultimate shear strength in slender webs from 129 previously published experimental tests. The results indicated that the models based on the Cardiff approach provided the best overall accuracy but required significantly more calculation effort to predict the interaction of the tension field with the flanges. Models based on Basler's approach provided a good blend of accuracy with relative simplicity since flange anchorage is neglected. Despite the general effectiveness of these foundational models, White and Barker's evaluation also revealed significant variation in the predictions from each model when applied across all 129 tests. Specifically, substantial standard deviations were calculated, and several outlier cases had tested shear resistances that were 25–120% larger than the model predictions. Though generally conservative, all models also had some predictions that were 10–25% lower than the lowest quartile of the test results [5].

In a recently published paper, new web shear buckling tests by Scandella et al. [8] on slender plate girders also showed reasonable agreement with Basler-based models for post-buckling shear capacity. The results of these tests indicated that the formation of a plastic mechanism per the current Eurocode/Höglund model did in fact mobilize some additional resistance and shear deformation ductility once the buckled web began to yield. In their study, Scandella et al. [8] suggested a generalized 3-stage breakdown of the shear response of slender webs in plate girders, which is illustrated in Fig. 2 and adapted for this study as follows:

1. *Linear Elastic Stage*: When shear loading is initially applied, the web plate undergoes small deformations and exhibits linear elastic resistance. Minor out-of-plane deformations occur due to the presence of initial imperfections; however, this state would generally be considered to be a "pure shear" response. The end of this stage is reached at a proportional shear limit, denoted as $V_p$ in Fig. 2, at which point web shear buckling behavior becomes more prominent.
2. *Post-buckling Stage I*: The web plate undergoes noticeable shear buckling, though not necessarily as a sudden bifurcation due to the presence of initial out-of-plane imperfections. Rather, the web settles into its buckled shape (depending on the magnitude and contour of initial imperfections) and increasingly deforms across the orthogonal compression diagonal both in-plane (which now has reduced stiffness relative to the tension diagonal) and out-of-plane (thus generating second-order bending in the buckled shape). The diagonal tension field load path becomes increasingly prominent due to its larger stiffness relative to the compression diagonal. The shear displacement of the panel exhibits progressively less stiffness than during the linear elastic stage until the buckled web panel begins to develop a plastic mechanism at $V_m$ in Fig. 2.
3. *Post-buckling Stage II*: The stiffness of the shear load-displacement response reduces significantly after the buckled web develops a plastic mechanism. The yielded, post-buckled web panel increasingly engages the flanges and stiffeners as its own shear stiffness reduces. Shear deformations rapidly increase until a failure mechanism is reached via extensive web yielding, plastic hinging in the flanges, and/or exhausting the resistance of the stiffeners. Fig. 2 illustrates three potential modes of Post-buckling Stage II response:
   - o *Stage II-A*: The shear resistance increases at a reduced rate (i.e. positive hardening) after the formation of the plastic mechanism at the end of Post-buckling Stage I. Ultimate shear load is reached at the peak of shear resistance during this stage (at $V_{u,II\text{-}A}$ in Fig. 2), after which the shear resistance descends toward failure.
   - o *Stage II-B*: The shear resistance reaches a local peak following the initial formation of the plastic mechanism at the end of Post-buckling Stage I and then slightly decreases. The shear resistance then recovers to develop additional shear resistance due to contributions from flange and/or stiffener support as well as hardening of the yielded, post-buckled web. A subsequent peak of shear resistance during this stage after significant deformation may or may not exceed that achieved at the end of Post-buckling Stage I. The representative example in Fig. 2 shows the ultimate shear load ($V_{u,II\text{-}B}$) being reached at the subsequent peak due to post-yield hardening recovery.
   - o *Stage II-C*: Ultimate shear load is achieved at the end of Post-buckling Stage I (i.e. $V_{u,II\text{-}C} = V_m$ in Fig. 2), after which the shear resistance descends as deformation increases toward eventual failure of the web panel. A post-ultimate mechanism that involves the flanges and/or stiffeners has developed but is unable to support any post-yield increase in shear resistance past the end of Post-buckling Stage I.

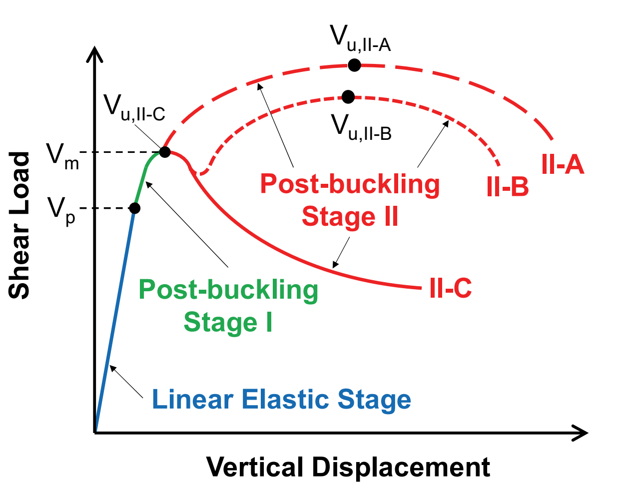


**Fig. 2.** Illustration of vertical load-displacement for a 3-stage web shear buckling response.

This 3-stage illustration provides a consistent, generalized description of web shear post-buckling response that can incorporate the mechanics used in all prevailing tension field models. Rather than simply trying to apply a single theory to a majority of cases, this approach instead recognizes that the post-buckling response of a particular plate girder design (particularly the mode of Post-buckling Stage II response) will depend on the relative sizing of the web, flange, and transverse stiffener plates. Both Lee et al. [35] and Scandella et al. [8] observed from previous test literature that a substantial flange thickness relative to the web thickness would be needed to provide the mechanism anchorage suggested by the Cardiff approach (Fig. 1c) and develop ultimate shear resistance per Post-buckling Stage II-A. Likewise, the stiffener would be needed to mobilize the mechanical model proposed by Höglund (Fig. 1d). White and Barker's aforementioned evaluation of published post-buckling models [5] noted that several of the 129 tested girders achieved ultimate shear loads that were significantly larger than the Basler-based model predictions. This suggests that ultimate shear strength for those cases may have been enhanced by the formation of a flange/stiffener mechanism via Post-buckling Stage II-A or II-B due to the sizing of those plates relative to the web. This study will therefore parametrically examine the influence of the flanges and transverse stiffeners on the mode of the Post-buckling Stage II response.

## 3. Modeling approach

The following objectives were used as the basis for the FE modeling approach in this study:

- FE predictions of ultimate shear resistance must not vary from those recorded in the experimental tests by more than ±10%, and preferably less.
- The vertical shear load-displacement behavior of the FE model should have good overall agreement with that from the test.
- The FE model should exhibit the same post-buckling deformed shape as the test specimen.
- Stress-strain relationships used as input for the steel material should resemble that obtained from coupon tests during each experimental program. In particular, realistic inelastic nonlinearity should be included in any prediction of post-buckling response [36].
- Out-of-plane imperfections in the web should be appropriately representative of the initial imperfections that were observed in the tested web plates, if measured [37].

### 3.1. Girder prototypes

Fig. 3 shows the respective dimensions, support conditions, and locations of load application for the "Basler" [16,17] and "Hansen" [18,19] test specimens. Web shear buckling behavior was targeted toward the "test section" web portion in the middle of each girder, which has constant shear and minimizes moment per the diagrams shown in Fig. 4. The web slenderness (equal to the clear depth between the flanges, $h$, divided by the web thickness, $t_w$) in the test sections was 267 for the Basler girders and 250 for the Hansen girders. Outside the test section, the web was substantially thicker (and Basler et al. included additional stiffeners) to prevent unintended web shear deformation. The transition between web thicknesses was made via a welded butt joint and was placed at the longitudinal ends of the test section in the Hansen girders. In the Basler girders, the thinner web plate was extended 304.8 mm beyond the extent of the test section for added web-shear continuity.

Each of the six tested specimens was outfitted with equally spaced vertical intermediate stiffeners (not shown in Fig. 3 for simplicity) that were welded to the web to impose a particular web panel aspect ratio in the test section. Basler girders were tested with aspect ratios of 1 (specimen G7) and 1.5 (specimen G6), and the Hansen girders were tested with aspect ratios of 1 (G1), 1.333 (G2), 2 (G3), and 4 (G4). The intermediate stiffeners in the test section had dimensions of 101.6 mm × 6.35 mm for the Basler girders and 70 mm × 3 mm for the Hansen girders. Larger bearing stiffeners were provided at all loading and reaction locations, and Basler et al. also reinforced the flanges at these locations with additional cover plates. All stiffeners in the Hansen girders were full-depth and fully welded to the web and flange interfaces. For the Basler girders, the same applied for all stiffeners outside the test section. The intermediate stiffeners in the Basler test sections were only welded to the web and to the compression flange (i.e. there was a 25.4-mm gap between the unwelded end of these intermediate stiffeners and the tension flange face). In all specimens, all stiffeners were installed symmetrically on both sides of the web centerline.

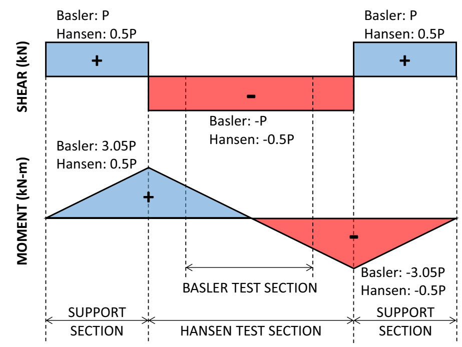


**Fig. 4.** Generic shear and bending moment diagrams for the as-tested girder configurations (note that vertical load P corresponds to the force arrows shown in Fig. 3).

### 3.2. Finite element model setup

The girder specimens were modeled in Abaqus 2017 [38] using S4R shell elements with seven integration points (following the Simpson integration rule) through their thickness. Isometric views of some of the discretized FE models (which include equally spaced intermediate stiffeners in the test section) are provided in Fig. 5. The girders were

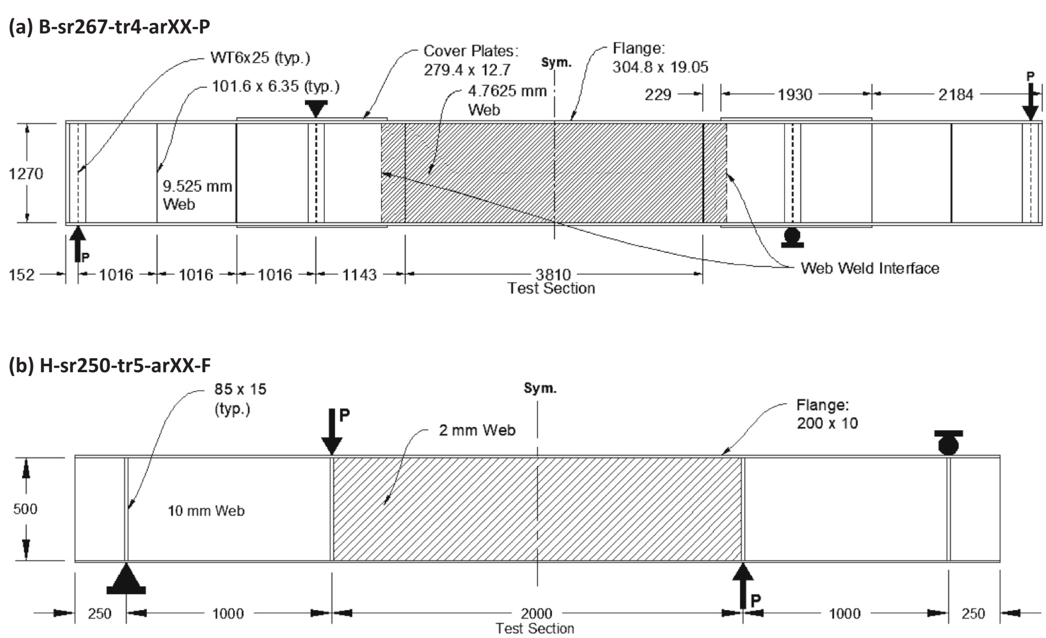


**Fig. 3.** As-tested girder configurations per (a) Basler et al. [16,17] and (b) Hansen [18,19] (all dimensions in mm). Note that intermediate transverse stiffeners within the test sections are not shown for clarity.

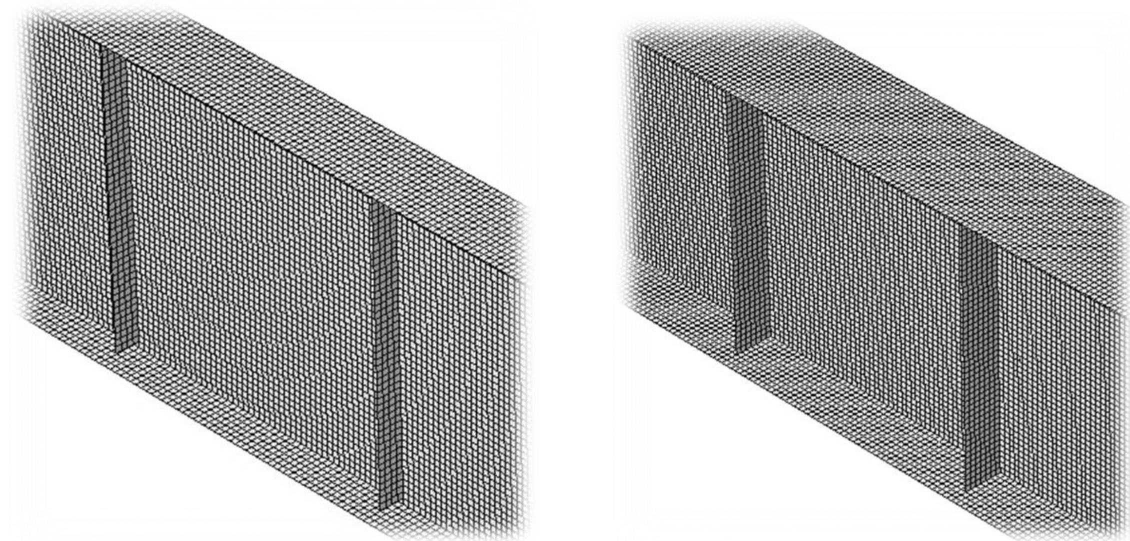

(a) B-sr267-tr4-ar1-P (b) H-sr250-tr5-ar1-F

**Fig. 5.** Isometric close-up view of a stiffened web panel in the discretized test sections of two as-tested FE model configurations.

meshed such that all shell elements were approximately square and the webs had 50 elements over their depth between the flanges. Similar element edge dimensions were used in the meshes of the flanges and stiffeners. This mesh density is similar to that used by the authors in their previous work on this topic [9,30,39,40] and was confirmed to be adequate via preliminary convergence analyses.

The vertical extent of the web elements is set equal to the web depth $h$ between the interior flange faces as shown in the Fig. 3 schematics. Welds between plates were modeled using a tie constraint between all degrees of freedom at co-located nodes. As a result, the flange element nodes (which are co-located with those of the web elements at their interface) are placed at $\pm h/2$ from the longitudinal mid-height centerline of the web. The on-center separation between the top and bottom flange elements is therefore reduced from $h + t_f$ in Fig. 3 to $h$ in the FE models, which will naturally have a slight impact on the strong-axis flexural resistance of the girder. However, the flexural bending effects are purposefully minimized per Fig. 4 in order to focus on shear response. Also, the web shear resistance is negligibly impacted by this simplification, as will be demonstrated in the validation of these models against the test results later in Section 4.

Again for simplicity, the vertical point loads were applied to a single node at the intersection of the bearing stiffener, web, and flange in order to mitigate localized deformation due to the concentrated force. All boundary conditions were applied to a single line of nodes across the full width of the flange at the applicable location. Out-of-plane (i.e. transverse) translation was restrained only at the locations of load application and vertical support.

The results of tensile coupon tests performed during each test program were used to develop true stress-strain ($\sigma_{true}$ vs. $\varepsilon_{true}$) relationships as steel material input for the FE models. For example, the engineering stress-strain ($\sigma_{eng}$ vs. $\varepsilon_{eng}$) curves in Fig. 6 for steel grades A36 (Basler et al. [16]) and S235 (Hansen [18]) correspond to tensile coupons from the test section web material and can be converted to true stress-strain via the following [41]:

$$\sigma_{true} = \sigma_{eng} \cdot \left(1 + \varepsilon_{eng}\right) \tag{1}$$

$$\varepsilon_{true} = ln\left(1 + \varepsilon_{eng}\right) \tag{2}$$

The A36 true stress-strain curve in Fig. 6 is based on the only coupon test reported for these girder specimens by Basler et al. [16] and is

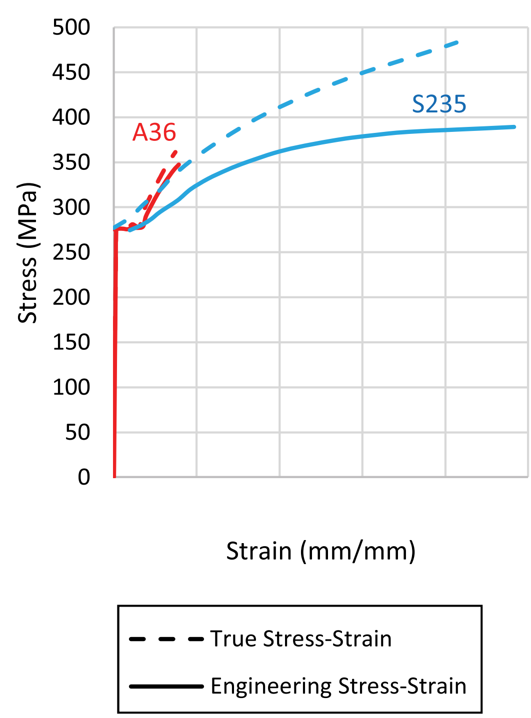


**Fig. 6.** Stress-strain relationships from tensile coupons of A36 [16] and S235 [18] steel material used for the tested girder webs.

therefore assigned to all plate components in the corresponding FE models as a simplification. Hansen, on the other hand, also reported coupon test results for the flange and stiffener plates [18] – true stress-strain curves for each plate type (though not plotted in Fig. 6 for brevity since they were similar) were therefore assigned to the corresponding components in the Hansen FE models. Poisson's ratio was set to a constant value of 0.3 for all cases.

The following naming convention will be used to identify the models in this paper: setup-sr#-tr#-ar#-F/P/V. The experimental "setup" indicates either the Basler (Fig. 3a) or Hansen (Fig. 3b) test configuration. The terms "sr", "tr", and "ar" denote the following:

- sr = web slenderness ratio, equal to web depth, *h*, divided by web thickness, $t_w$
- tr = flange-to-web thickness ratio, equal to the flange thickness, $t_f$, divided by web thickness, $t_w$
- ar = aspect ratio of the stiffened web panels in the test section, equal to longitudinal panel length, *a* (measured on center between stiffeners), divided by web depth, *h*

The last term of "F", "P", or "V" describes the stiffener boundary conditions:

- F = a full depth stiffener that is welded to the web and both flanges (i.e. Hansen's test section design [18]).
- P = a stiffener which is welded only to the web and compression flange, clipped 25.4 mm away from the tension flange (i.e. Basler et al.'s test section design [16]).
- V = the intermediate stiffeners in the test section have been replaced with a so-called "virtual" stiffener (i.e. an out-of-plane translational restraint is applied to every node along the removed stiffener's centerline over the full depth of the web).

The F and P cases will be used accordingly for FE model validation. The V stiffener condition will be used later in this paper to further examine the role of the stiffener in the post-buckling mechanics of the web panel. By replacing the stiffener with an out-of-plane translational restraint, the virtual stiffener offers no axial resistance during post-buckling but provides the web test section with rigidly defined panelization.

The FE analyses are performed via a two-step process. First, the eigenmodes of each plate girder are determined using the "buckle" analysis in Abaqus with an idealized girder geometry, which has a flat web and no imperfections. The load at which the first positive eigenmode is achieved is designated as the elastic or critical buckling load, $V_{cr}$. The shape of the first eigenmode is then scaled relative to a predefined maximum amplitude and imposed onto the initially undeformed girder geometry as an initial imperfection. The first-eigenmode displacement in the flanges, stiffeners, and web plates outside the test section are much smaller than those within the test section, where the thinner web plate experiences the most initial imperfection. Previous studies by the authors [30,39] and others [37,42,43] have also used scaled first eigenmode web displacements to reasonably represent realistic initial imperfections in FE models that capture post-buckling behavior in slender webs.

In the second step of FE analysis, the girder with initial imperfections is subjected to numerically stabilized quasi-static loading via the Modified Riks analysis in Abaqus [44]. This method of analysis can obtain the full mechanical behavior of the girder from the linear elastic stage through the onset of post-buckling behavior until ultimate shear load is reached and the girder subsequently unloads toward numerical failure. The ultimate shear load is identified as the maximum value reached during the Modified Riks analysis. Recall that, per Fig. 2, the ultimate shear load can occur either at the end of Post-buckling Stage I (at which point the buckled web panel begins to form a plastic mechanism) or during Post-buckling Stage II (if the plastic mechanism develops positive hardening, thus enabling a subsequent gain or recovery of shear resistance as deformations rapidly increase).

For model validation, the maximum amplitude of the initial imperfections is scaled to *h/100*, which emulates the maximum out-of-plane web imperfection allowed by current design standards [2,4]. The *h/100* imperfection magnitude has been commonly used for FE modeling in previous studies on this topic [43,45] as an upper bound value for initial out-of-flatness of a built-up plate girder in practice. Some modeling strategies have also used initial imperfections of this magnitude to implicitly account for the effects of welding-induced residual stresses near the web-to-flange interfaces [37], since these stresses are often neglected in this type of FE analysis for simplification (including those presented in this paper). Fig. 7 compares the out-of-plane web imperfections that were recorded prior to Basler et al.'s girder tests [17] to those imposed on the corresponding FE models via *h/100* scaling of the first positive eigenmode deformation. The proposed imperfections provide a reasonable (and generally conservative) representation of the measured values in terms of both shape and magnitude. Measurements of initial imperfections were not reported for the Hansen girders [18], and *h/100* scaling of the first eigenmode is therefore assumed as an upper bound imperfection for model validation. Later in Section 4.4 of this paper, the influence of the imperfection magnitude will be further examined for the FE models of all as-tested girder cases.

## 4. Model validation

### 4.1. Shear load-displacement: Basler girders

Based on available data, three comparisons are made between the experimental and FE results for the two Basler girders: (1) vertical load vs. displacement at the point of load application in Fig. 3a, (2) out-of-plane web displacement measured at several locations by Basler et al. [17], and (3) the post-buckled deformed shape. Recall that for the Basler test setup, the applied load is equal to the shear load on all panels in the test section (see Fig. 4). Fig. 8 shows close agreement between the experimentally measured vertical load-displacement curves up to their termination and the corresponding configurations of the FE models (ar1-P and ar1.5-P). Note that only one curve is shown in Fig. 8 for each case – the experimental and modeled displacements both correspond to the loading location at which the larger displacements were measured (i.e. on the side of the specimen at which a more prominent web shear buckling response was observed). Per Basler et al.'s test report [17], the ar1 test was pushed past the ultimate shear load (i.e. the maximum shear value reached during the test) into a gradually descending branch; however, the test was stopped before an accelerated drop in resistance could be reached. The ar1-P model shows the same gradual descent of shear load past ultimate and subsequently experiences a more rapid drop in resistance just beyond the termination of the test curve (at roughly 3× the displacement at which ultimate shear was reached).

Basler et al.'s ar1.5 test was unfortunately stopped just after ultimate shear load was reached [17], at which point the loading was relieved and additional intermediate stiffeners were welded to the buckled web for subsequent load tests (the results of which are not the focus of this study). The ar1.5-P model shows a similarly gradual descent of shear load past ultimate as compared to the ar1-P case until an accelerated drop in resistance at roughly 4× the displacement at which ultimate was reached. The slight increase in post-ultimate ductility from ar1 to ar1.5 reflects the decreased shear stiffness of the test section panelization with the larger aspect ratio. Per Fig. 2, the load-displacement curves for both specimens exhibit a Post-buckling Stage II-C response, having reached ultimate shear resistance at the end of Post-buckling Stage I and experiencing no additional increase or recovery of shear resistance during Post-buckling Stage II.

The red as-tested FE curves in Fig. 8 (for cases B-sr267-tr4-arX-P) include milestone markers that denote major transitions in shear stiffness. The red diamonds mark the point at which the shear stiffness decreases to zero, indicating the ultimate shear state as well as the end of Post-buckling Stage I via the onset of a plastic mechanism. The red circles mark the point at which the rate of negative stiffness in the descending branch begins to accelerate during the Post-buckling Stage II-C response. Fig. 8 also includes curves for additional iterations of the Basler FE models that were analyzed with either full-depth ("F") or virtual ("V") intermediate stiffeners in the test section for comparison. Recall that for the V cases, all intermediate stiffeners over the thinner web section in Fig. 3a are replaced with out-of-plane translational restraint. For further examination, an additional F case was analyzed in which the thickness of the intermediate stiffeners was arbitrarily increased by a factor of 5 (referred to as case "F5"). In Fig. 8, all stiffener

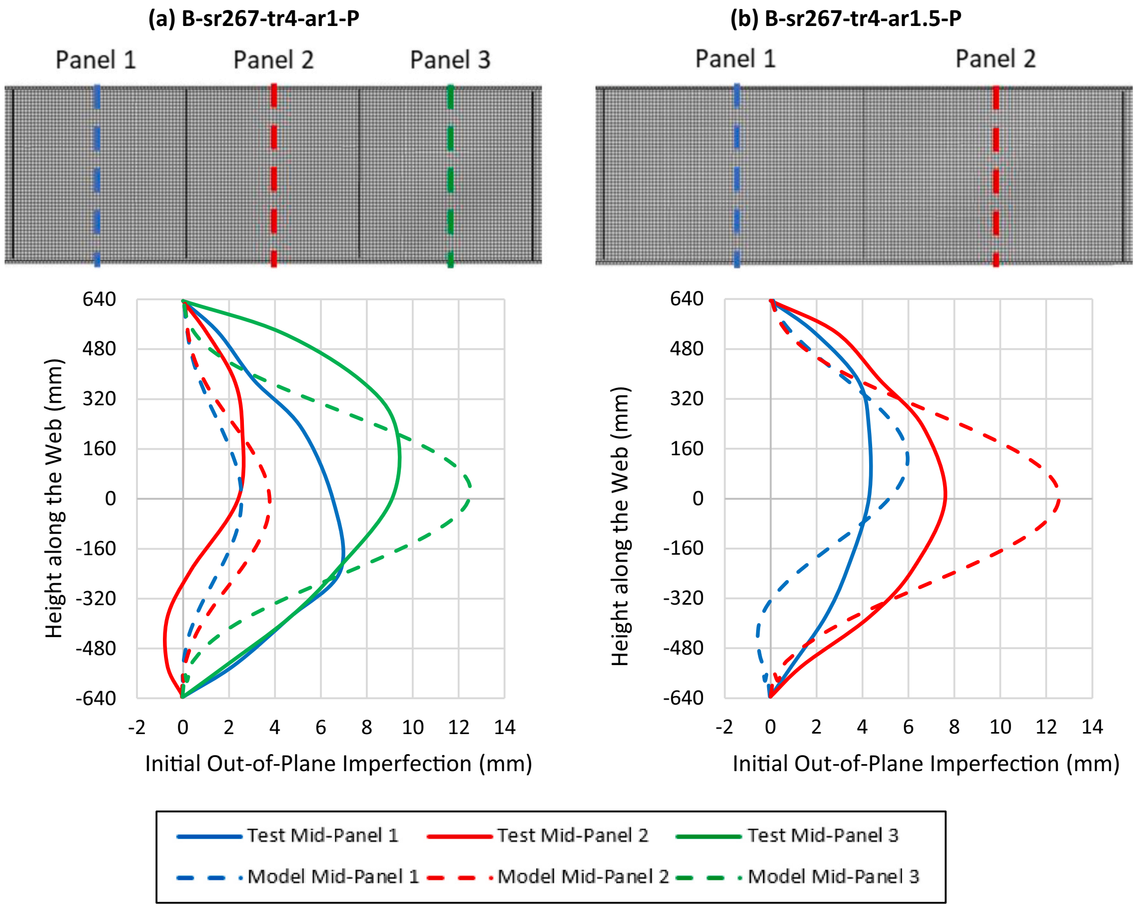


**Fig. 7.** Initial out-of-plane imperfections in the web test sections of the Basler girders: experimental measurements [17] versus the FE models' first positive eigenmode (scaled to a h/100 maximum amplitude).

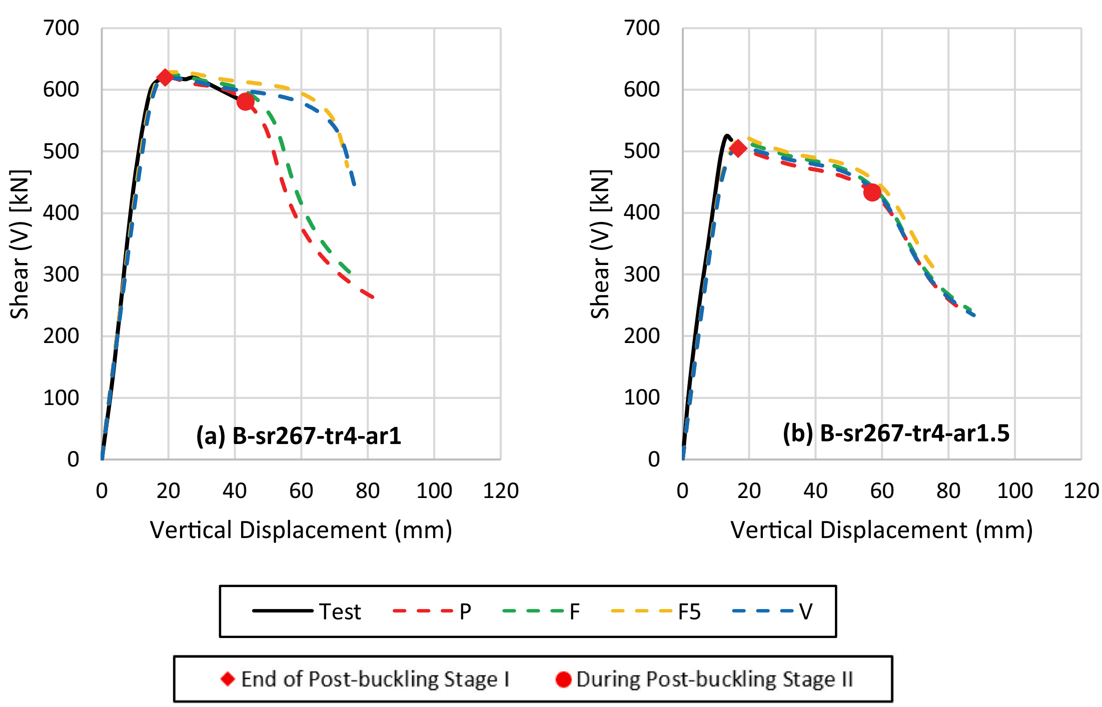


**Fig. 8.** Shear ($V$) versus vertical displacement at the applied load locations for the Basler girders.

variation cases (P, F, F5, and V) exhibited similar Post-buckling Stage II-C responses with nearly the same ultimate shear resistance $V_u$ from Modified Riks analysis with h/100 first-eigenmode initial imperfections. Fig. 9 summarizes these values of $V_u$ as well as the critical buckling loads $V_{cr}$ (obtained from the initial eigenmode "buckle" analyses), which are also nearly identical among all stiffener iterations.

In Fig. 8, the shear load-displacement results for the F stiffener cases of both girders are nearly identical to those of the as-tested P cases, indicating that the full depth stiffener made a negligible additional contribution to the web shear mechanics throughout Post-buckling Stages I and II. For the ar1.5 models in Fig. 8b, the shear load-displacement for the F5 and V cases are also nearly identical to those of the P and F iterations, indicating that the post-buckling response of the ar1.5 web panels was not sensitive to these variations in the axial resistance or the degree of out-of-plane restraint provided by the stiffeners. For the ar1 models in Fig. 8a, the response of the F5 and V cases is very similar to the P and F cases past the end of Post-buckling Stage I but then maintains a higher shear resistance in the latter half of Post-buckling Stage II-C before a rapid descent toward numerical failure. The ar1 web panels therefore experienced some slight improvement in their Post-buckling Stage II-C response due to the increased out-of-plane restraint from the F5 and V stiffeners. Axial engagement of the stiffener does not appear to significantly influence these responses since the F5 and V cases offer drastically different amounts of axial stiffener resistance (i.e. a five-fold increase versus zero).

Fig. 10 compares the deformed shapes of the tested girders (shown via post-test photos) with those from the as-tested (P stiffener) FE models. The photo of the ar1 (i.e. G7) test specimen after a full Post-buckling Stage II-C response closely resembles the corresponding shape of the ar1-P model, with both showing the formation of a flange hinge mechanism in the rightmost web panel. A photo of the ar1 specimen at ultimate shear was not provided in Basler et al.'s test report. The shape of the ar1-P model at ultimate shear clearly shows the formation of diagonalized web buckling but does not yet show visual evidence of a flange or stiffener anchorage mechanism at the end of Post-buckling Stage I.

Recall that the ar1.5 test was stopped just after having reached ultimate shear (see Fig. 8b). The post-test photo in Fig. 10 therefore corresponds to the ultimate shear state and compares well with the corresponding deformed shape of the ar1.5-P model. Again, these images do not visually indicate a mechanism that involves flexural flange or axial stiffener anchorage of the tension field. A post-ultimate photo of the ar1.5 specimen was not available since the specimen was unloaded, modified, and retested after ultimate shear was reached in the initial test. However, the shape of the ar1.5-P FE model during Post-buckling Stage II again shows the formation of a flange anchorage mechanism in the rightmost panel, similar to the ar1-P model.

Fig. 11 plots the out-of-plane displacement measured at the web locations marked in Fig. 10. All curves account for initial imperfections and generally show good agreement as the shear load is applied and the panels undergo post-buckling behavior. The only exception is Point 3 for the ar1 girder, at which the first eigenmode *h/100* initial imperfection in the FE model fell on the opposite side of the web centerline compared to the measured value. However, the absolute value of the FE initial imperfection and the subsequent shape of the shear vs. deflection history at that point were nearly identical between the experimental specimen and ar1-P model. Overall, all curves followed a similar trend of out-of-plane deflection up to ultimate shear. Fig. 8a showed that the ar1-P test and model both initially exhibit linear behavior until a slight decrease in slope at approximately $V = 500$ kN. Near this shear load, all points at the middle of the three ar1 panels in Fig. 11 also show varying increases in out-of-plane displacement as the web enters Post-buckling Stage I and progresses toward the ultimate shear load. The ar1.5-P test and model show a similar transition from linear elastic to Post-buckling Stage I at approximately $V = 450$ kN in Fig. 8b, and Points 1 and 2 in the ar1.5 panels show a corresponding increase of out-of-plane displacement in Fig. 11. After reaching ultimate shear and progressing into the panel mechanism during Post-buckling Stage II, the out-of-plane displacements at Point 3 in the rightmost ar1 panel and Point 2 in the rightmost ar1.5 panel show the largest increases in out-of-plane displacement (consistent with the deformed shapes shown previously in Fig. 10).

### 4.2. Shear load-displacement: Hansen girders

Fig. 12 plots the shear load vs. vertical displacement from the FE models of the as-tested Hansen girders at both locations of load application per Fig. 3b against those recorded during each test. Note that for the Hansen test setup, the shear load (*V*) is equal to half the vertical load (*P*) on all panels per Fig. 4. Also, the load-displacement for the ar2 girder was not reported due to an instrumentation error during that test [18]. The other three girder cases show close agreement in the initial linear elastic stage and Post-buckling Stage I before experiencing a significant change in slope as the buckled web panels yield and transition to Post-buckling Stage II. The ar4 results (Fig. 12d) continue to show close agreement throughout the Post-buckling Stage II-C response as the web panel develops a ductile mechanism and gradually unloads from ultimate at the end of Post-buckling Stage I. The transition to Post-buckling

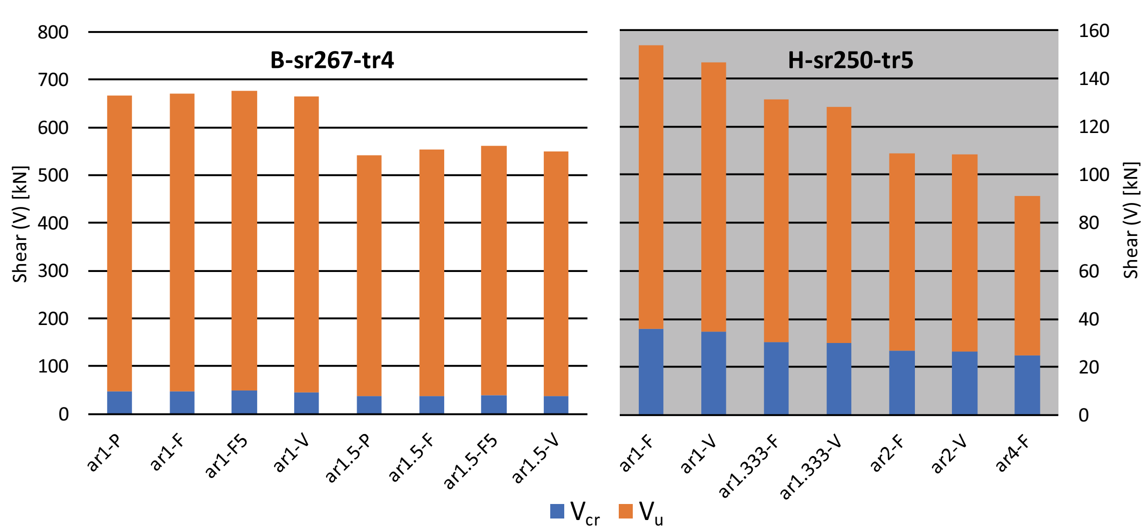


**Fig. 9.** Ultimate and critical shear resistances from all FE models with varying stiffener configurations.

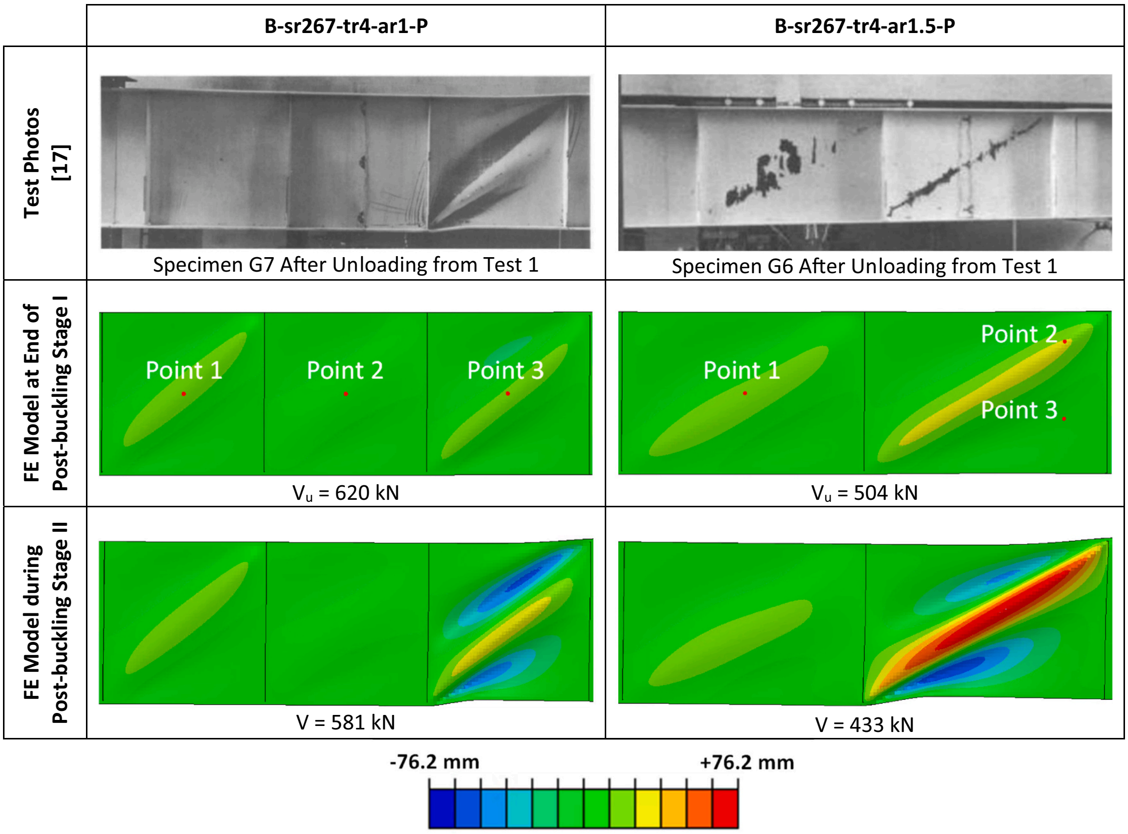


**Fig. 10.** Comparison of deformed shapes for the Basler girders: experimental photos (reproduced with permission from Fritz Laboratory at Lehigh University) versus the as-tested FE model configurations.

Stage II-A in the ar1 and ar1.333 girders (Fig. 12a-b) occurred at a slightly lower shear load in the test results than in the FE results, and the experimental Post-buckling Stage II-A response showed a slightly more rapid increase in deformation. These differences can be attributed to the fact that the Hansen girder tests were conducted using a manual load-controlled actuator system, for which the rate of loading was not consistent for each test [18]. As a result, the experimental curves would be expected to show a more rapid transition to reduced stiffness in Post-buckling Stage II than a displacement-controlled approach, such as the Modified Riks method used for the FE analyses [46].

Cases with virtual stiffeners were also analyzed, with all intermediate stiffeners again replaced with out-of-plane nodal translational restraint. Unlike the Basler V cases, however, the stiffeners at each longitudinal end of the test section was retained in the Hansen V models because they resisted direct bearing from the applied load per Fig. 3b. The Hansen ar4 model, which has no other intermediate stiffeners in its web test section, was therefore not analyzed with a V stiffener condition. Similar to the Basler girders, Fig. 9 showed that the values of ultimate shear resistance are again nearly identical for the F and V stiffener iterations of each Hansen girder. The load-displacement behavior of the Hansen ar2-V case in Fig. 12 shows particularly good agreement with the as-tested F model, as both exhibit a Post-buckling Stage II-C response. The ar1.333-V Post-buckling Stage II-A behavior in Fig. 12b is also relatively close to that of its corresponding F case and reaches only a slightly lower ultimate shear value. These results (similar to those for both Basler girders) suggest that the Post-buckling Stage II response for these web panels with rectangular aspect ratios do not necessarily rely on the physical stiffener for axial resistance but rather for out-of-plane restraint.

The Hansen ar1-V model shows similar behavior as its corresponding F case in Fig. 12a up to the end of Post-buckling Stage I; however, it is unable to develop the same Post-buckling Stage II-A response. The ar1-V case exhibits a sudden dropoff in shear resistance early in Post-buckling Stage II before it can reach the same ultimate shear value as the ar1-F model. For the 2-mm thick Hansen web with a square aspect ratio, the axial resistance provided by the physically present stiffener therefore contributes to the development of a post-yield hardening increase of shear resistance. However, it should be noted that the mobilization of post-yield hardening is dependent on the relative and raw thicknesses of the web, stiffener, and flange plates. Recall that the Basler ar1 models were all unable to develop post-yield hardening regardless of their stiffener configuration. The Basler and Hansen girders have nearly the same slenderness ratio, but the Basler web is 2.4 times thicker with a 20% lower flange-to-web thickness ratio. Parametric analyses presented in Sections 4 and 5 of this paper will further explore the influence of these plate sizes on the mode of Post-buckling Stage II (i.e. post-yield) response.

The red as-tested FE curves in Fig. 12 again include markers for the end of Post-buckling Stage I (diamond) and during Post-buckling Stage II (circle). The deformed shapes of the as-tested Hansen girder FE models at these two milestones are shown in Fig. 13 and are very similar to the specimen photos provided in Hansen's test report [18]. All FE models of the Hansen girders showed very little flange deformation at the end of Post-buckling Stage I (including ar2-F and ar4-F, which reached ultimate shear at this milestone). The deformed shapes during Post-buckling Stage II (when ar1-F and ar1.333-F reached ultimate shear) clearly show an increase of out-of-plane web deformation as well as increased flexural deformation in the flanges. These images visually demonstrate that the varying degrees of web and flange deformation from Post-buckling Stage I to Stage II do not necessarily provide an explicit indication of the ultimate shear state.

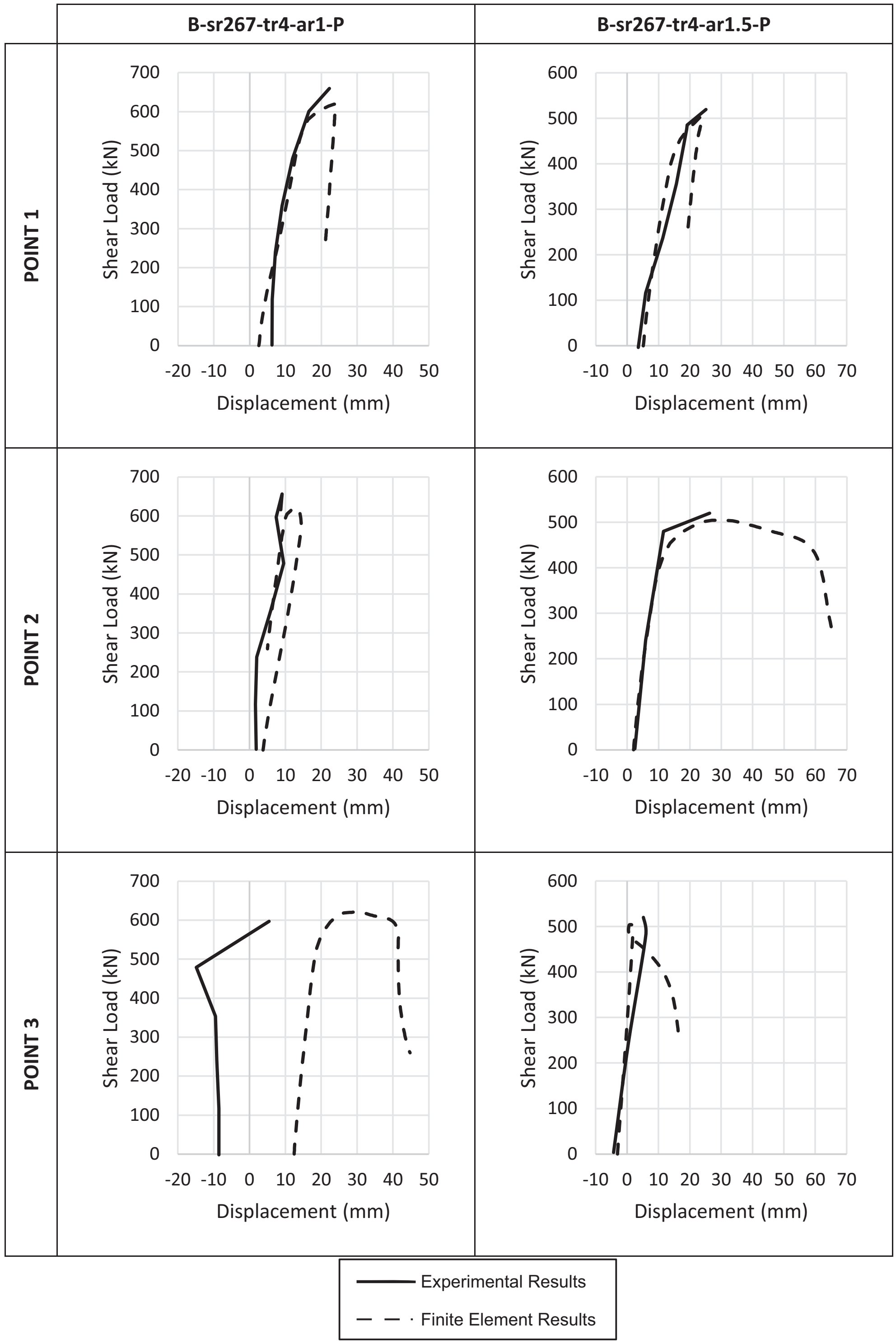


**Fig. 11.** Out-of-plane web displacement histories for the as-tested Basler girders.

### *4.3. Sensitivity to material input*

As shown previously in Fig. 6, the steel material used in the Basler and Hansen tests had similar yield strength but drastically different post-yield hardening, ultimate strength, and ultimate ductility per the reported coupon test results. To confirm that the shear load-displacement behavior in Fig. 8 and Fig. 12 was not unduly influenced by the post-yield ductility of these materials, the stress-strain material inputs were swapped between the validation FE models, which were then reanalyzed for comparison. For simplicity, the entirety of both Basler models were assigned the true stress-strain curve from Hansen's S235 web coupons, and the Hansen models were likewise given Basler et al.'s singular A36 true stress-strain curve. Fig. 14 shows that the material swap had little influence on most of the FE shear load-displacement results. The Basler ar1 and ar1.5 models both experienced very small increases in ultimate shear resistance when using the more ductile S235 material. In the Hansen ar1 and ar1.333 models, the ultimate strength was reached at a slightly greater displacement in Post-buckling Phase II-A when the A36

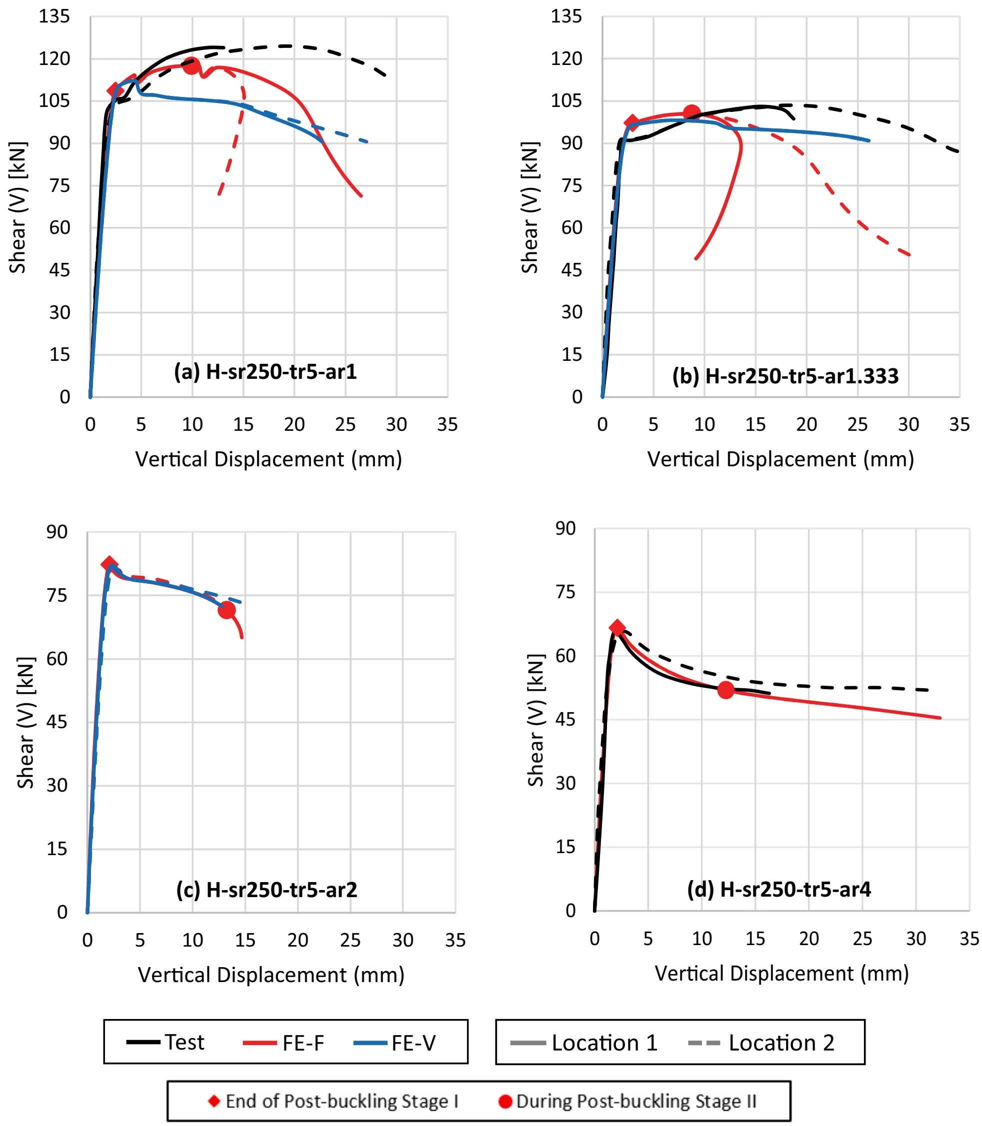


**Fig. 12.** Shear ($V$) versus vertical displacement at the applied load locations for the Hansen girders.

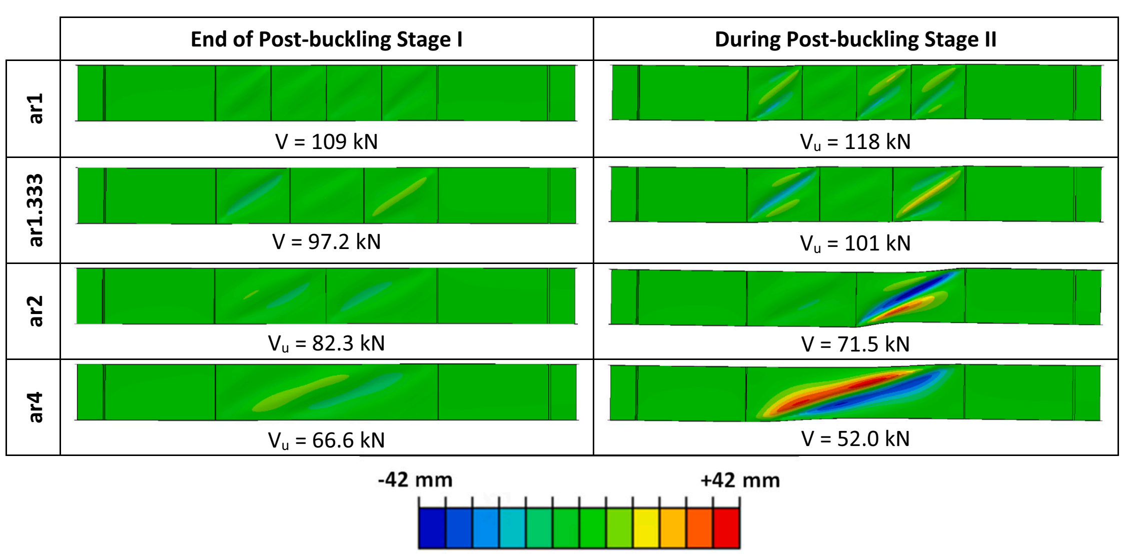


**Fig. 13.** Deformed shapes of the as-tested Hansen FE models (H-sr250-tr5-arX-F).

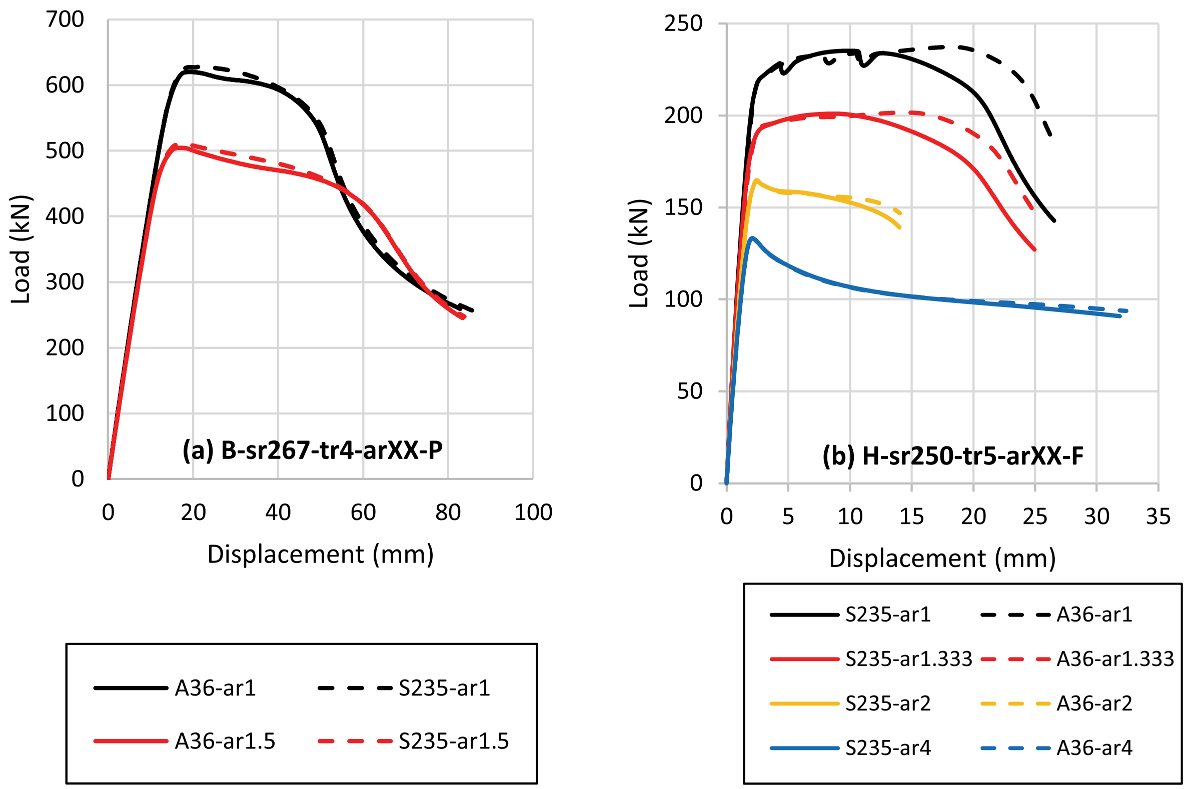


**Fig. 14.** Comparison of shear (*V*) versus vertical displacement at the applied load locations: (a) Basler and (b) Hansen FE models using both stress-strain relationships from Fig. 6 as steel material input.

material was used.

In these cases, the steeper positive hardening stiffness of the A36 material may have slightly increased the initial resistance of the web panel's post-yield mechanism. However, the overall behavior for all cases was otherwise nearly identical when using either material model. Further exploration of these material effects is outside the scope of this study, and the FE models presented in the rest of this paper will therefore continue to pair each FE model with its corresponding stress-strain relationships.

### *4.4. Sensitivity to initial imperfection magnitude*

To examine their sensitivity to initial imperfection magnitude, all FE models of the as-tested girder configurations were re-analyzed with the same first eigenmode shape but with reduced maximum scaling of *h/1,000* and *h/10,000*. The load-displacement plots in Fig. 15 (which include the *h/100* curves from Fig. 8 and Fig. 12) show that all girder models have very little sensitivity to the magnitude of the initial imperfection. The *h/100* models show only slightly less elastic stiffness compared to those with smaller imperfections, and the ultimate shear

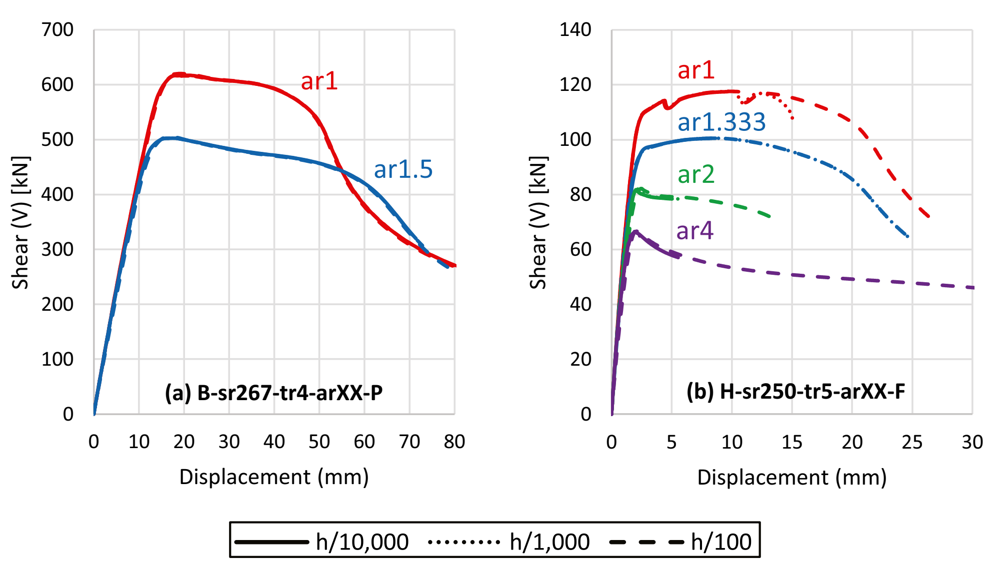


**Fig. 15.** Shear (*V*) versus vertical displacement at the applied load locations for the as-tested (a) Basler and (b) Hansen FE models with varying initial imperfection magnitudes in the web test section.

and overall shape of the load-displacement curves after Post-buckling Stage I are unchanged. The only significant consequence of decreasing the imperfection magnitude was a reduction in post-ultimate ductility before reaching numerical non-convergence. With smaller imperfections, the web plate experiences slightly more in-plane "locking" in its post-buckled state, leading to a more rapid onset of localized yielding and numerical instability during Post-buckling Stage II. In particular, the Hansen FE models with the smaller imperfections showed much post-buckling post-yield ductility due to the thinness of its test section web plate compared to the Basler web test section. Up to the point of numerical non-convergence, though, the analyses displayed very similar results. The rest of this study therefore proceeds with the *h/100* scaling of the first eigenmode shape because it was able to capture similar levels of post-ultimate ductility as the experimental tests.

The level of consistency among these models has also been demonstrated in other studies that examined the sensitivity to similar ranges of initial imperfection magnitude for FE models of complete plate girders (which included the flanges, stiffeners, and multiple web panels similar to this study) [45,47]. Studies that instead utilized FE models of single web panels with idealized boundary conditions [29,43,48] showed a more demonstrable decrease in both elastic shear stiffness and ultimate shear capacity as the imperfection magnitude was increased.

### 4.5. Comparison with code-based strength predictions

The ultimate shear strength (i.e. the maximum shear value in each shear-displacement history in Fig. 8 and Fig. 12) from each test as well as from each as-tested FE model configuration (with *h/100* initial imperfections and corresponding material input) are summarized in Table 1. The results show good overall agreement, with no more than 8% deviation from the test results. Also, the FE predictions are conservative for all cases with ar $<$ 2.

Table 1 also includes code-based predictions per Chapter G of AISC 360–16 [3] and Section 5 of Eurocode 3, Part 1–5 [4]. The code-based calculation procedures (including a list of variables) are summarized in the appendix at the end of this paper. Recall that for ar $\leq$ 3, the AISC approach for stiffened webs uses tension field equations based on Basler [15] with no explicit flange contribution. For ar $>$ 3, the AISC equations are based on Höglund's rotated stress theory [34] but again with no direct flange contribution. The EC3 approach for stiffened webs with rigid intermediate stiffeners is also based on Höglund's rotated stress theory but includes a calculated contribution from the flanges. It is important to note that the stiffeners of all girder cases met the requirements for "rigid" intermediate stiffeners per EC3; per AISC 360–16, however, the stiffeners all passed the flexural stiffness requirement but failed the minimum width-to-thickness requirement. Despite this, the tests and FE models of all girder cases successfully exhibited shear buckling behavior with no flexural or stability concerns in the stiffeners.

Similar to the FE models, all code-based calculations used the reported material strengths from tensile coupon tests during each experimental program as input rather than nominal design strengths. The results of all calculations therefore compare the predictive capabilities of each model by using the same material strength input. The code-based models do not explicitly state whether the calculated shear resistance is targeted toward $V_u$ regardless of the mode of Post-buckling Stage II response or instead toward the shear value at end of Post-buckling Stage I when the plastic mechanism has developed (i.e. at $V_m$ in Fig. 2, which coincides with $V_{u,II\text{-}C}$ but not $V_{u,II\text{-}A}$ or $V_{u,II\text{-}B}$). For the purpose of this study, the code-based predictions are compared against the experimental and FE values of $V_u$ regardless of the mode of Post-buckling Stage II response.

The AISC predictions of shear resistance ($V_n$) showed close agreement with the ultimate experimental values for all girder cases with ar $\leq$ 2, with all predictions less than 10% conservative and similar to the corresponding FE values. These results suggest that the web shear buckling response in both the tests and FE models of the ar $\leq$ 2 girder cases can be quantified via tension field action in the web per Basler [15] with relatively little direct flange contribution. For H-sr250-tr5-ar4-F, however, the AISC prediction was 31% conservative after transitioning to Höglund's rotated stress theory but with no flange contribution. Conversely, the EC3 prediction ($V_{b,Rd}$) for H-sr250-tr5-ar4-F was nearly identical to the test result and the FE value, suggesting that the flange contribution was increasingly significant for the ar4 case. For all girder cases with ar $<$ 2, the EC3 predictions were more conservative (by margins of 6–26%) than their AISC counterparts. For H-sr250-tr5-ar2-F, the FE results and both code-based predictions all showed good agreement with the experimental ultimate shear. This confluence of predictions creates ambiguity as to whether the flange contributions were significant for the Hansen ar2 girder, since those contributions are explicitly calculated in the EC3 approach, neglected in the AISC approach, and are inherently part of the full-girder FE model. Further examination of the flange contributions to the ultimate strength of the as-tested prototype girders will therefore be presented in more depth in Section 6 of this paper.

## 5. Intermediate stiffener participation

The internal axial force in the intermediate stiffeners in the web test section were obtained from the FE analyses of all stiffener iterations for the Basler and Hansen girder models. For P and F cases, Abaqus' "free body cut" command was used to record the net vertical (axial) force at the mid-height of each stiffener (i.e. by cutting through all symmetric stiffener shell elements on opposite sides of the web). For V iterations, the free body cut was taken across the four web elements at the mid-depth of the web that straddle the virtual stiffener's vertical centerline.

The axial force at ultimate shear is reported in Table 2 for each intermediate stiffener (numbered from left to right across the web test section) as well as the left and right end stiffeners shown in Fig. 3. First, it should be noted that the end stiffeners of all Hansen model iterations show high values of compression (at about ~75% of the applied shear) since they are engaged in direct bearing at the applied load location in Fig. 3b. Because these stiffeners act as bearing stiffeners, their results are not pertinent to our study of intermediate stiffener participation but are included in Table 2 for completeness.

All other stiffeners in every model iteration have low values of axial load relative to the ultimate shear load. Specifically, the values of

**Table 1**
Summary of shear resistance for all as-tested girder configurations.

| Model Name | Exp. [17,18] | FEM | | AISC [3] | | EC3 [4] | |
|---|---|---|---|---|---|---|---|
| | $V_u$ (kN) | $V_u$ (kN) | FEM/Exp. | $V_n$ (kN) | AISC/Exp. | $V_{b,Rd}$ (kN) | EC3/Exp. |
| B-sr267-tr4-ar1-P | 663 | 620 | 0.94 | 640 | 0.97 | 474 | 0.71 |
| B-sr267-tr4-ar1.5-P | 529 | 504 | 0.95 | 513 | 0.97 | 407 | 0.76 |
| H-sr250-tr5-ar1-F | 125 | 115 | 0.92 | 113 | 0.90 | 95.1 | 0.76 |
| H-sr250-tr5-ar1.333-F | 103 | 101 | 0.98 | 97.5 | 0.95 | 91.7 | 0.89 |
| H-sr250-tr5-ar2-F | 79.5 | 82.3 | 1.04 | 75.8 | 0.95 | 78.4 | 0.99 |
| H-sr250-tr5-ar4-F | 66.1 | 66.6 | 1.01 | 45.9 | 0.69 | 66.6 | 1.01 |

**Table 2**
Axial force at mid-height of each transverse stiffener over the web test section at ultimate shear.

| Model Name | $V_u$ (kN) | Axial Force (kN) at $V_u$ [as a % of $V_u$] Left End | Interm. #1 | Interm. #2 | Interm. #3 | Right End |
|---|---|---|---|---|---|---|
| B-sr267-tr4-ar1-P | 620 | -24.1 [3.9%] | -66.6 [10.7%] | -55.6 [9.0%] | - - | -25.5 [4.2%] |
| B-sr267-tr4-ar1-F | 624 | -29.6 [4.8%] | -66.0 [10.6%] | -66.3 [10.6%] | - - | -29.4 [4.7%] |
| B-sr267-tr4-ar1-F5 | 629 | -43.8 [7.0%] | -86.8 [13.8%] | -86.2 [13.7%] | - - | -43.7 [6.4%] |
| B-sr267-tr4-ar1-V | 620 | 3.5 [0.6%] | -38.0 [6.1%] | -38.0 [6.1%] | - - | 3.4 [0.6%] |
| B-sr267-tr4-ar1.5-P | 504 | -8.1 [1.6%] | -17.4 [3.5%] | - - | - - | -6.9 [1.4%] |
| B-sr267-tr4-ar1.5-F | 515 | -34.7 [6.7%] | -87.8 [17.1%] | - - | - - | -36.7 [7.1%] |
| B-sr267-tr4-ar1.5-F5 | 523 | -62.0 [11.9%] | -154.0 [29.5%] | - - | - - | -66.1 [12.6%] |
| B-sr267-tr4-ar1.5-V | 507 | -12.7 [2.5%] | -51.8 [10.2%] | - - | - - | -6.7 [1.3%] |
| H-sr250-tr5-ar1-F | 118 | -85.9[a] [72.8%] | -28.7 [24.3%] | -34.0 [28.8%] | -39.4 [33.4%] | -87.3[a] [74.0%] |
| H-sr250-tr5-ar1-V | 112 | -78.5[a] [66.6%] | -2.8 [2.5%] | -4.6 [4.1%] | -3.5 [3.1%] | -81.3[a] [72.6%] |
| H-sr250-tr5-ar1.333-F | 101 | -71.1[a] [70.4%] | -23.2 [23.0%] | -23.6 [23.4%] | - - | -73.5[a] [72.8%] |
| H-sr250-tr5-ar1.333-V | 98.2 | -69.8[a] [71.1%] | -1.6 [1.6%] | -1.7 [1.8%] | - - | -71.8[a] [73.1%] |
| H-sr250-tr5-ar2-F | 82.3 | -62.7[a] [76.2%] | -17.8 [21.6%] | - - | - - | -64.0[a] [77.7%] |
| H-sr250-tr5-ar2-V | 82.0 | -63.0[a] [76.8%] | -7.8 [9.5%] | - - | - - | -64.1[a] [78.1%] |
| H-sr250-tr5-ar4-F | 66.6 | -51.3[a] [77.0%] | - - | - - | - - | -52.4[a] [78.7%] |

[a] *Bearing stiffeners.*

stiffener axial load do not exceed 34% in any case, averaging 9% among the Basler P/F/F5 configurations and 26% for the Hansen F configurations. All V model iterations exhibited even smaller values of axial force in the web elements at the virtual stiffener mid-height, averaging 4% and not exceeding 10% of the ultimate shear. Collectively, these results indicate that the girders are not utilizing the transverse stiffeners (or in the V cases, the web elements at the virtual stiffener locations) to the extent that would be expected for a load path mechanism that emulates a Pratt truss. This corroborates the commentary in AISC 360–16 which states that the axial forces in intermediate stiffeners are not significant compared to the forces they experience in providing out-of-plane restraint and panelization to the web plate [3].

### *5.1. Axial stiffener response: Basler girders*

As expected, the axial forces in the Basler intermediate stiffeners increase slightly with the transition in configuration from P to F to F5. The addition of contact to both flanges provided a modest ~20% increase for ar1.5-F but negligible change for ar1-F. The subsequent 5× increase of the stiffener thickness for both ar1-F5 and ar1.5-F5 attracted ~50% more axial force. The replacement of the physical stiffener with the virtual stiffener decreases the vertical axial load at the stiffener location by at least half versus the as-tested P configurations. Again, all model iterations reached nearly the same ultimate shear resistance (see Fig. 9) and exhibited similar Post-buckling Stage II-C responses (see Fig. 8).

Fig. 16 plots the growth of stiffener axial forces for the as-tested P configurations as a function of the applied shear force. The following milestones are marked with vertically dashed lines: BLUE is during the linear elastic stage (taken at $V_{cr}$); GRAY is at the end of Post-buckling Stage I (marked with a red diamond in Fig. 8); and BLACK is during Post-buckling Stage II (marked with a red circle in Fig. 8). All curves are terminated at the last milestone (during Post-buckling Stage II) for improved clarity in the Fig. 16 plots. Beyond this point, the stiffeners around the yielded panel tend to increase in compression as the panel deformations accelerate, and all other stiffeners unload.

The curves in Fig. 16 reveal that the compression in each stiffener increases proportionally with applied shear until peaking when shear reaches about 95% of $V_u$, after which the stiffener axial force begins to rapidly decline. At ultimate shear, the end stiffeners decline to much smaller values (i.e. near zero), while the other intermediate stiffeners decline about 12% from their peak values as the post-buckling yield mechanism is formed (at the transition from Post-buckling Stage I to Stage II). The peak values plotted in Fig. 16 are still much lower than the corresponding value of applied shear and again do not emulate a vertical strut load path in a Pratt truss. After ultimate shear during the Post-buckling Stage II-C response, the axial force in each stiffener in Fig. 16 settles to a compressive value no greater than 25 kN for either the ar1-P or ar1.5-P models. This indicates that the web and flanges have a more prominent role than the stiffeners in developing the Post-buckling Stage II response of these girder configurations.

### *5.2. Axial stiffener response: Hansen girders*

Compared to the Basler girders, Fig. 17 shows a relatively similar increase of stiffener compression versus applied shear for the as-tested Hansen F configuration models through most of the initial linear elastic stage and Post-buckling Stage I. However, these curves show a continual increase of stiffener compression all the way to the end of Post-buckling Stage I. For the ar2 and ar4 cases (Fig. 17c-d), ultimate shear is reached at this milestone, after which the stiffener compression backtracks slightly as the panel yields during Post-buckling Stage II-C. However, the post-ultimate decrease in stiffener compression is significantly less than what was shown for the as-tested Basler models in Fig. 16. The thinner web in the Hansen models has much less stiffness to resist post-buckling deformation than the thicker Basler web – as a result, the Hansen stiffeners were more engaged in compression during Post-buckling Stage II-C after ultimate shear was reached.

For the as-tested ar1 and ar1.333 Hansen cases in Fig. 17a-b, the stiffener compression continues to increase through the end of Post-buckling Stage I until reaching ultimate shear during Post-buckling Stage II-A. At the end of Post-buckling Stage I, the rate of increase in stiffener compression accelerates in ar1 but stagnates somewhat in ar1.333. However, neither case shows a decrease in stiffener compression during Post-buckling Stage II-A, indicating that the stiffeners are actively engaged to support the hardening increase in shear resistance after the onset of the post-buckling yield mechanism. Recall that for the Hansen ar1 case, the replacement of the physical F stiffener with the virtual V stiffener adversely impacted the web panel's ability to fully develop a Post-buckling Stage II-A response, as shown in Fig. 12a. For the Hansen ar1.333 case, however, the same replacement had much less impact on its Post-buckling Stage II-A shear-displacement response in Fig. 12b. The increased reliance of the Hansen ar1-F case on the stiffeners during post-yield hardening in Post-buckling Stage II-A is reflected in Table 2, in which the Hansen ar1-F stiffeners are shown to have ~20% more axial force than the Hansen ar1.333-F stiffeners when measured relative to their respective ultimate shear values.

Also shown in Table 2, the as-tested Hansen ar1-F and ar1.333-F models developed about 2–3 times the amount of axial force as a percentage of ultimate shear versus the as-tested Basler ar1-P and ar1.5-P, which have similar web panel aspect ratios. This clearly indicates that

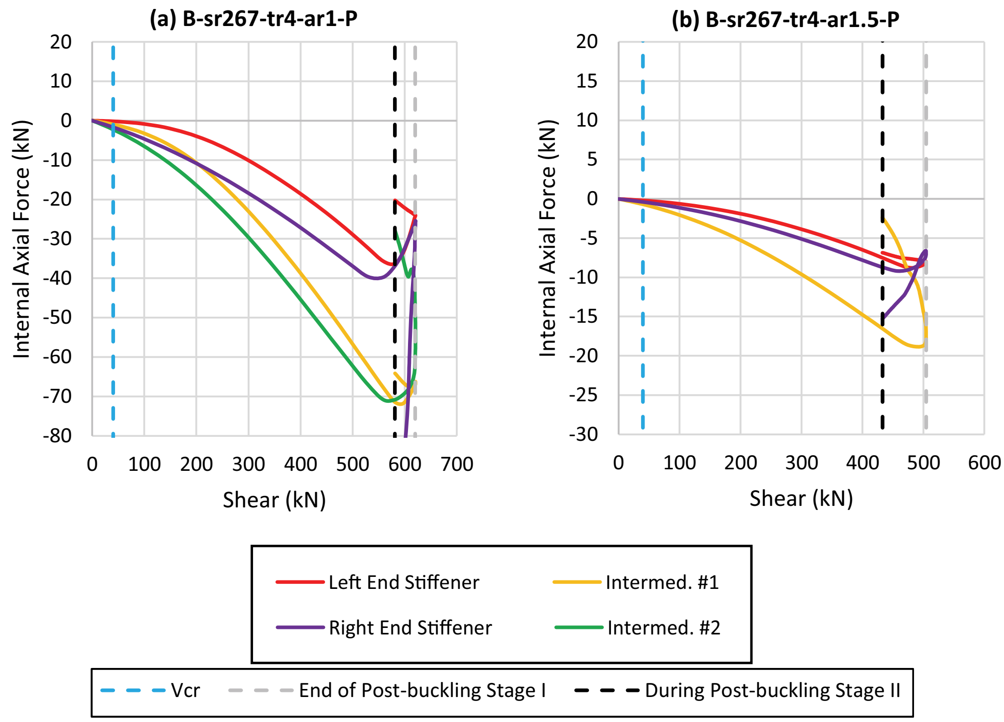


**Fig. 16.** Mid-height axial forces in the test section stiffeners of the as-tested Basler FE models versus applied shear.

the stiffeners generally played a larger role in the post-buckling mechanics of the thinner Hansen web plate, which have less second-order resistance against continued deformation of its buckled shape in compression diagonal direction. Despite this, the Hansen ar1-F and ar1.333-F girders both showed no change in shear load-displacement behavior between their F and V stiffener cases in Fig. 12a-b before the formation of the plastic web panel mechanism at the end of Post-buckling Stage I. This further indicates that the initial development of the post-buckling yield mechanism relied on the stiffeners more for out-of-plane restraint rather than for axial resistance, even for cases with an elevated level of axial stiffener utilization during post-yield hardening.

## 6. Flange contributions

Up to this point, all analyses presented in this paper have used flange-to-web thickness ratios (tr) that correspond to the as-tested girder configurations (i.e., tr4 for the Basler girders and tr5 for the Hansen girders). To examine the contributions of the flange plates to post-buckling shear behavior, the as-tested FE models were re-analyzed with varying flange thicknesses, such that the flange-to-web thickness ratio was systematically increased from two (tr2) to seven (tr7) in single unit increments. All other dimensions, material inputs, and stiffener properties were unchanged from the as-tested FE model configurations that were introduced in Section 3.2. All models in this range of tr2 to tr7 experienced ductile web shear buckling behavior with no local instability in the flanges or stiffeners. Additional analyses whose results are not presented here exhibited flange instability at $tr < 2$ (due to a combination of local flexure and axial compression) or instability of the intermediate stiffeners at $tr > 7$ (due to very high flange stiffness, which prevented flange hinging and subsequently distributed more compression to the stiffeners during the transition to Post-buckling Stage II).

### 6.1. Impacts to shear load-displacement

For illustration, the relationships of shear load versus vertical displacement are plotted in Fig. 18 for the tr2, tr4, and tr6 iterations of the Basler and Hansen girders (all other cases are not shown here for brevity, since the plotted cases are adequate for establishing relevant trends of behavior). As expected, the Hansen ar4 cases in Fig. 18f showed much less sensitivity to the changes in flange-to-web thickness ratio due to the lower impact of tension field behavior on its post-buckling response. Otherwise, the results clearly show that an increased flange-to-web thickness ratio enables a progressively higher value of $V_u$ as well as slightly higher initial stiffness during the linear elastic stage and Post-buckling Stage I prior to the formation of a plastic mechanism. The post-yield shear resistance during Post-buckling Stage II can also be enhanced by the increased flange thickness. In particular, girder cases with $ar \leq 2$ transition from Post-buckling Stage II-C to II-A (i.e. ultimate shear is now reached during Post-buckling Stage II instead of at the end of Post-buckling Stage I) once their flanges are enhanced to tr6. The increased flange thickness therefore provides not only a more robust anchorage for the tension field but also a stiffer out-of-plane and torsional boundary condition at the top and bottom of the web throughout the web-shear response.

### 6.2. Impacts to ultimate shear resistance

The ultimate shear resistances achieved for all increments of tr2 to tr7 are summarized in Fig. 19. All values are normalized by the ultimate shear value from the as-tested version of the model (i.e., B-ar267-tr4-arX-P for the Basler girders and H-ar250-tr5-arX-F for the Hansen girders). The ultimate shear changed by no less than −22% at tr2 and no more than +19% at tr7 versus the ultimate shear resistance of the as-tested model configuration across all girder cases. The girders with $ar < 2$ showed greater sensitivity to the changes in flange thickness, since those girders have more tension field engagement and would therefore derive more benefit from enhanced flange anchorage. In particular, the Hansen ar1 and ar1.333 cases showed the widest range of variation due to the thinness of their web plate and the increased reliance on the stiffener and flange to develop ultimate shear and a post-buckling plastic mechanism. The Hansen ar4 case again showed some of the least sensitivity due to its lower level of tension field engagement. The Basler cases lost no more than −8% of ultimate shear at the tr2 lower bound. At the tr7 upper bound, the Basler cases were able to increase their ultimate

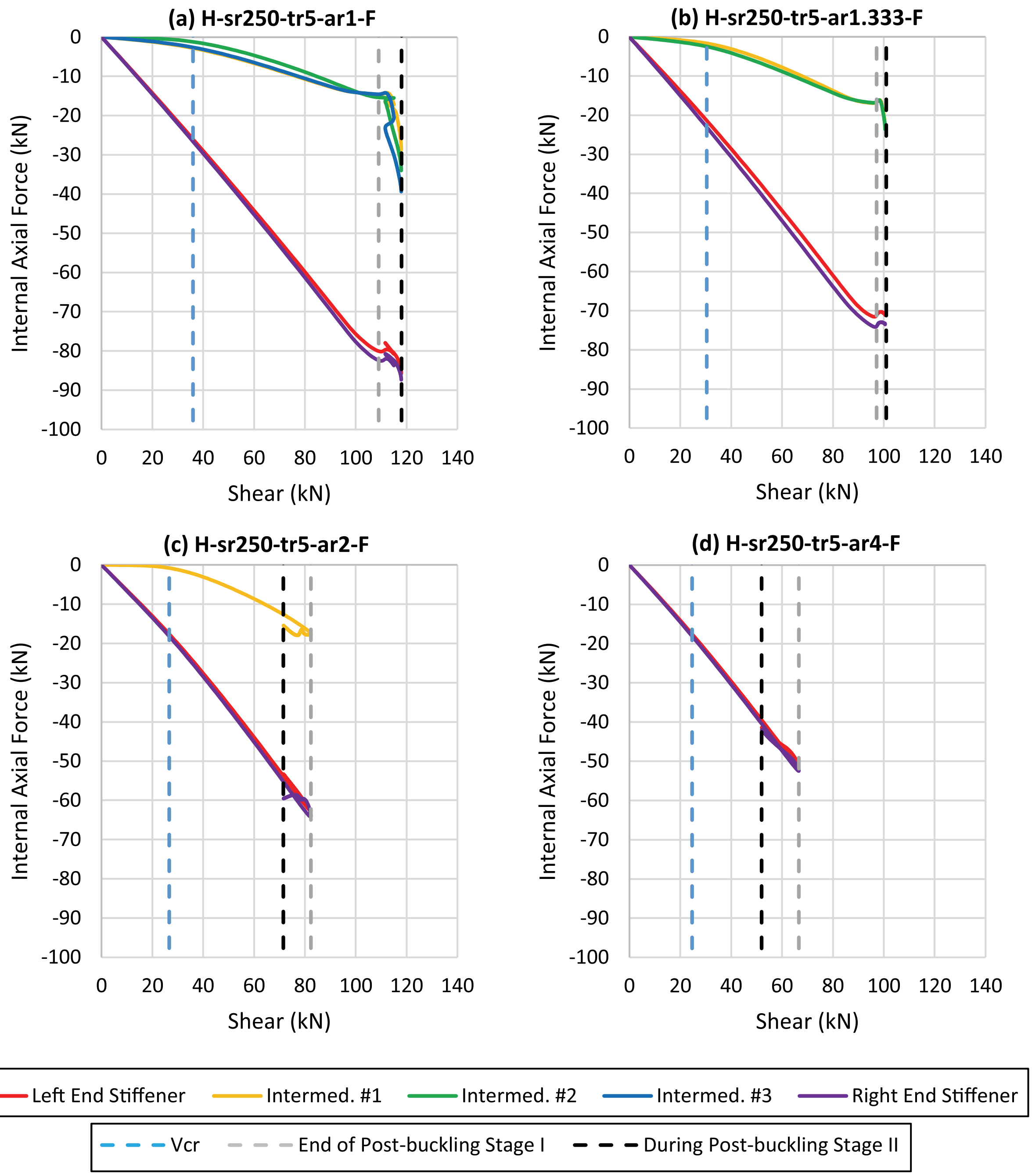


**Fig. 17.** Mid-height axial forces in the test section stiffeners of the as-tested Hansen FE models versus applied shear.

shear resistance by +9% (ar1.5) and +19% (ar1) because the larger flange stiffness enhanced the Post-buckling Stage I response as well as the subsequent Post-buckling Stage II-A response.

### 6.3. Comparison with code-based strength predictions

Code-based predictions of shear strength are plotted in Fig. 20 for the tr2, tr4, and tr6 iterations of both Basler girder configurations (ar1 and ar1.5) as well as the ar1, ar2, and ar4 configurations of the Hansen girders (the ar1.333 Hansen case is not shown here for brevity). All code-based predictions are normalized by the ultimate shear value obtained from the corresponding FE model (denoted in Fig. 20 as $V_{u,FE}$). Recall that the AISC 360–16 predictions of shear resistance ($V_n$) for these prototypes is unaffected by the changes in flange thickness – the variation in the normalized AISC values plotted in Fig. 20 for each trX case is therefore only a function of the change in the FE model's ultimate shear. The EC3 prediction of shear resistance ($V_{b,Rd}$), however, directly accounts for a contribution from the flanges ($V_{bf,Rd}$) in addition to that of the buckled web ($V_{bw,Rd}$). The variation in the normalized EC3 values therefore accounts for changes in both the code-based prediction and the FE model ultimate shear for each trX case.

In Fig. 20, the two code-based predictions show opposite trends relative to the FE ultimate shear for these cases with varying tr values. Specifically, the AISC predictions become increasingly conservative as the tr value increases since they neglect the corresponding increase in flange contribution. Conversely, the EC3 predictions become less conservative and converge toward the FE ultimate shear as the tr value (and thus the flange contribution) increases. The EC3 approach especially outperforms the AISC prediction for the Hansen ar4 girder, since the AISC approach at this aspect ratio is using equations based on Höglund's

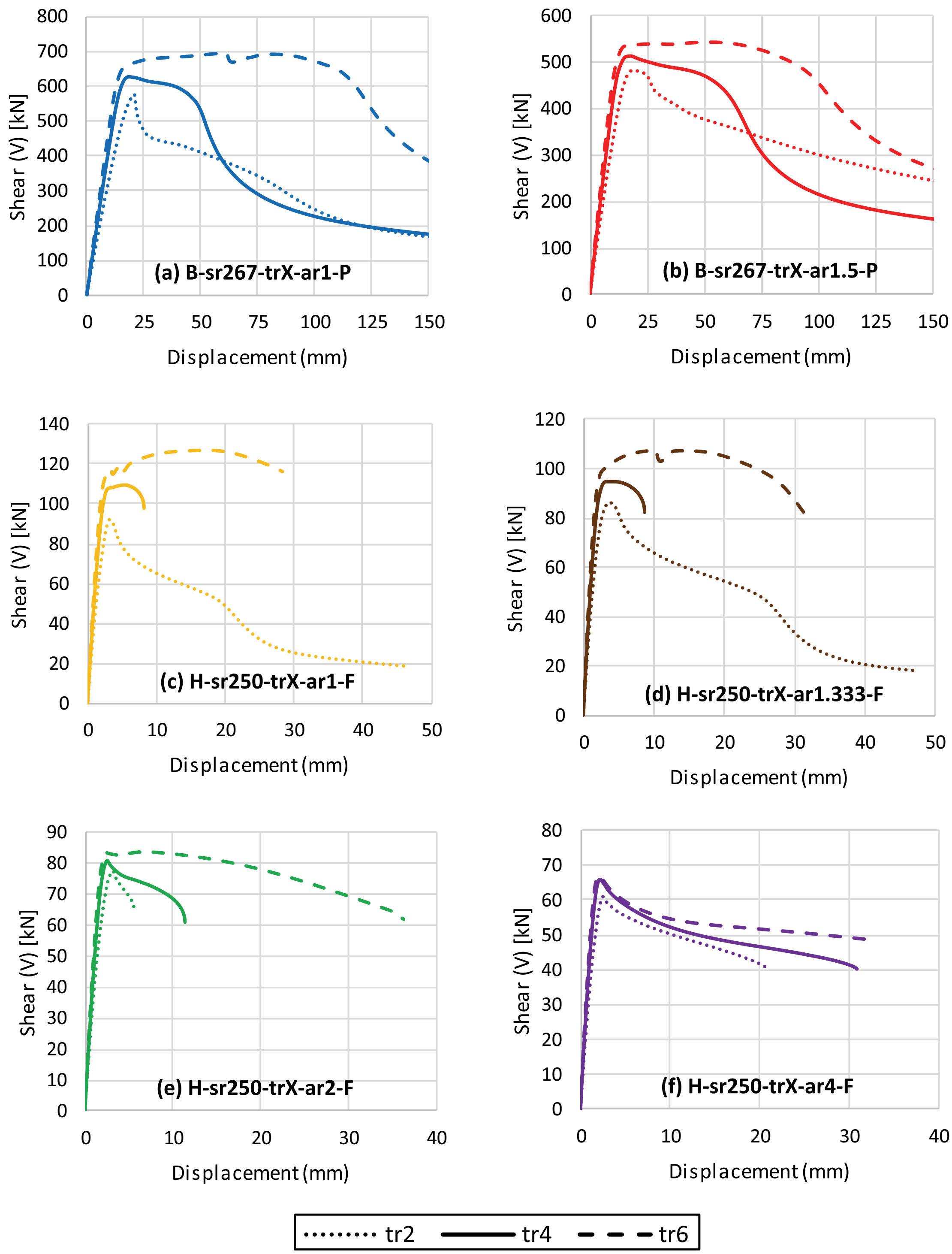


**Fig. 18.** Shear (*V*) versus vertical displacement at the applied load locations for FE models with varying flange-to-web thickness ratio (tr).

rotated stress theory (similar to EC3) but with no flange contribution. It is notable that neither code-based model is able to provide a consistently conservative prediction relative to the FE results across this array of girder configurations. To achieve such consistency, the mechanical models and assumptions behind the code-based models could be refined to fully capture the coupled contributions of the web, flanges, and stiffeners as demonstrated in these FE simulations. Additional experimentation and validated modeling would be needed to expand the comparison in Fig. 20 to a wider range of practical girder configurations.

### 6.4. Impacts to axial stiffener response

For further examination, the stiffener forces from the tr6 iteration of the Basler ar1-P model, which exhibits a Post-buckling Stage II-A response in Fig. 18a (similar to the as-tested Hansen tr5-ar1-F model in Fig. 12a), are plotted against the applied shear in Fig. 21. The results show a rapid increase in compression for intermediate stiffeners 1 and 2 during Post-buckling Stage II-A until ultimate shear resistance is reached, again similar to the intermediate stiffeners in the Hansen tr5-ar1-F model in Fig. 17a. The end stiffeners, however, show a similar

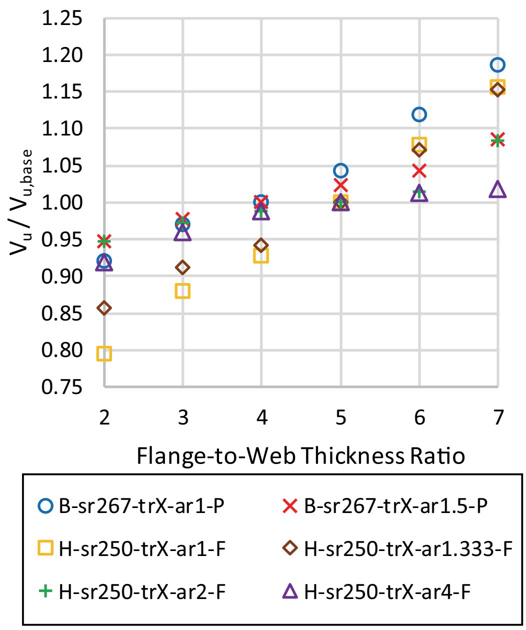


**Fig. 19.** Relationship between varying flange-to-web thickness ratio (tr) and $V_u$ (normalized by $V_{u,base}$ from the corresponding as-tested configurations).

decline in axial force as those in the as-tested Basler tr4-ar1-P model after the end of Post-buckling Stage I in Fig. 16a. The curves in Fig. 18 again suggest that a Post-buckling Stage II-A response will increasingly engage the intermediate stiffeners in compression. However, the maximum compression in the B-sr267-tr6-ar1-P intermediate stiffeners at the ultimate shear state still only reaches ~25% of the ultimate shear value.

## 7. Conclusions

This study leverages the published results of two previous test programs to examine the mechanics that develop in the buckled webs of slender steel plate girders in pure shear. The finite element (FE) modeling approach used in this study was able to effectively predict the load-displacement behavior, ultimate shear resistance, and post-buckled deformed shapes of all tested specimens. The validated models were then parametrically altered to examine the relative roles of the flanges and intermediate stiffeners in developing post-buckling behavior. The following conclusions can be drawn from the results of this study:

- FE models of full girder specimens tested previously at Lehigh University [15–17] ("Basler girders") and the Technical University of Denmark [18,19] ("Hansen girders") showed good agreement with test results by utilizing initial imperfections that scaled the first eigenmode of web shear buckling by a magnitude of *h/100*.
- The ultimate shear resistance and general load-displacement behavior of the FE models showed little sensitivity to reductions in initial imperfection magnitude to *h/1,000* or *h/10,000*. This is consistent with previous studies that utilized whole-beam models of plate girders. Other studies that modeled individual web panels under shear have shown more sensitivity to initial imperfections, especially pertaining to shear stiffness and ultimate shear resistance. Previous work by the authors [48] showed that the impact of large initial imperfections on web shear behavior will be mitigated by

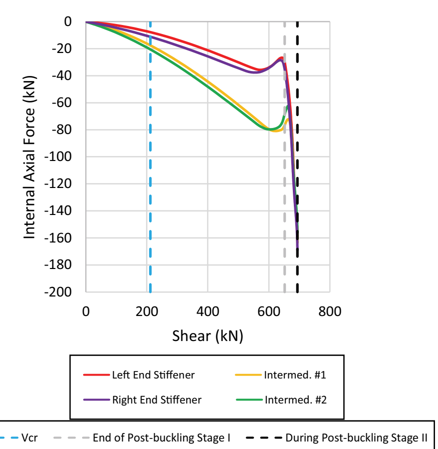


**Fig. 21.** Mid-height axial forces in the test section stiffeners of the B-sr267-tr6-ar1-P model versus applied shear.

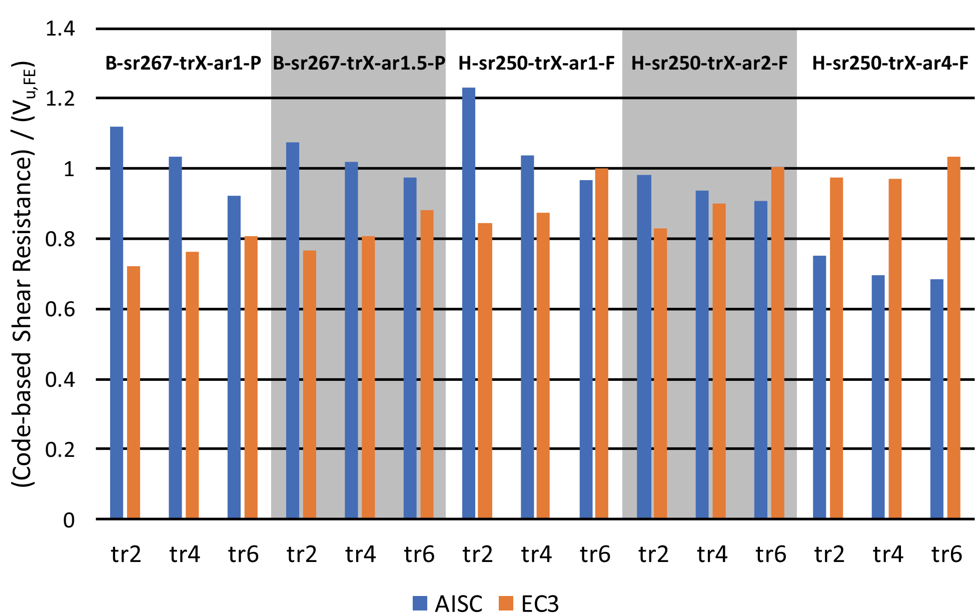


**Fig. 20.** Code-based predictions of shear resistance, normalized by the corresponding FE model ultimate shear resistance, for prototype girders with varying flange-to-web thickness ratio (tr).

extending the numerical models beyond the web panels that buckle to include more of the girder length. This ensures that the boundary conditions for the panels that buckle are provided by modeled structural elements rather than idealized, user-defined nodal restraints.

- The FE models and test results both showed that the girder specimens reached their ultimate shear strength at varying levels of displacement ductility. Specifically, all girders develop a plastic post-buckling mechanism in one or more of the stiffened web panels, but the relative sizing of the web, flange, and stiffener plates as well as the web panel aspect ratio will determine whether the shear resistance increases (via hardening) or decreases (via gradual unloading) once a post-buckling yield mechanism has developed.
- The following 3-stage response proposed by Scandella et al. [8] was shown to be a useful tool for understanding web shear buckling behavior: 1) an initial linear elastic stage, 2) Post-buckling Stage I during which shear stiffness begins to progressively decrease, and 3) Post-buckling Stage II with significantly reduced stiffness (after the buckled web panel has yielded in shear).
- The experimental and FE ultimate shear resistances were compared against predictions from two major code-based approaches. The AISC 360–16 approach for stiffened web panels with tension field action [3] (based on work by Basler et al. [15–17]) showed good overall agreement with the test results and were comparable to the FE results for panels with aspect ratios $\leq 2$. Among these cases, it is interesting to note that the Basler ar1 and ar1.5 cases as well as the Hansen ar2 case reached ultimate shear at the end of Post-buckling Stage I, while the Hansen ar1 and ar1.333 cases reached ultimate shear during Post-buckling Stage II at a much larger displacement. The Eurocode 3, Part 1–5 approach for stiffened panels with rigid transverse stiffeners [4] (based on Höglund's rotated stress theory [34] with contributions from both the buckled web and the flanges) showed better accuracy than the AISC approach for the Hansen girder cases with aspect ratios of 2 and 4, for which the ultimate shear was reached at the end of Post-buckling Stage I.
- The magnitude of axial compression in the intermediate stiffeners at ultimate shear were much less than would be expected for a structural system that emulates a Pratt truss. Stiffeners were engaged more so in bending to create the web panelization via out-of-plane restraint. Models that replaced the physical stiffeners with "virtual stiffeners" (i.e. a vertical line of out-of-plane translational restraint at the stiffener location with no vertical axial resistance) produced nearly identical predictions of critical buckling load and ultimate shear resistance as those with the physical stiffeners.
- By increasing the flange thickness (thus increasing its flexural and torsional stiffness), the ultimate shear resistance can be potentially achieved at much higher displacements past the point of post-buckled shear yielding. In those cases, the stiffeners also experienced an increase in compression after the formation of the yield mechanism as the web panel progressed toward ultimate shear. However, the increased ultimate shear resistance enabled by the enhanced post-yield hardening mechanism was only 5–10% greater than the shear resistance at the onset of post-buckled yielding (i.e. at the end of Post-buckling Stage I).
- Conversely, girder analyses with thinner flanges relative to the web thickness reached ultimate shear at the end of Post-buckling Stage I, and the compression in their intermediate stiffeners began to decline at that milestone. Girders with smaller web aspect ratios and/or thinner web plates exhibited the largest sensitivity to changes in the flange and stiffener boundary conditions.
- The AISC and EC3 predictions of shear resistance rely on varying assumptions regarding participation of the flanges and stiffeners to anchor the transfer of shear load in the buckled web. Neither code-based prediction provided a consistently conservative prediction of ultimate shear resistance versus the FE predictions when the thickness of the flange was varied relative to the web thickness. Specifically, the AISC predictions became increasingly conservative as the flange-to-web thickness ratio increased because it neglects the corresponding increase in flange contribution. Conversely, the EC3 predictions became less conservative and converged toward the FE ultimate shear as the flange-to-web thickness ratio (and thus the flange contributions) increased, especially for web panels with larger aspect ratios.
- To be more consistent with the plastic design philosophy inherent to modern codes [2–4], the shear resistance at the end of Post-buckling Stage I (i.e. $V_m$ in Fig. 2 when the plastic mechanism initiates in the post-buckled web panel) may be a more appropriate design target than $V_u$ (which, depending on the web panel boundary conditions, might be reached at large displacements well after the plastic mechanism has formed). Such an approach would ensure that the design shear value is reached prior to entering Post-buckling Stage II, thus neglecting any mode of post-yield behavior. The results of this study also indicate that the value of $V_m$ will be somewhat affected by flange anchorage to the web panel, and thus analytical expressions used to predict $V_m$ would preferably incorporate those contributions.

Note that the findings of this study are based upon two prototype girder geometries with large web slenderness ratios of 250–267. Slender plate girders in modern steel construction practice are commonly designed with slenderness ratios of 150 or lower [2,49,50]. Previous research by others has indicated that the findings in this paper are also applicable at lower ranges of web slenderness. For example, Wang et al. [48] also demonstrated low levels of axial engagement in the transverse stiffeners of a specific prototype girder (based on an FHWA design example [49]) which had a web slenderness of 138 and web panel aspect ratios ranging from 1 to 3. Previous work by Yoo and Lee [29] also demonstrated similar sensitivities of ultimate post-buckling shear strength due to varying flange thicknesses for a stiffened web with slenderness of 150. To further generalize these findings, a more comprehensive study is needed to parametrically evaluate both the stiffener engagement and flange contributions for web post-buckling behavior over a wider practical range of not only web slenderness but also web plate thicknesses at the same slenderness.

## Declaration of Competing Interest

The authors declare that they have no known competing financial interests or personal relationships that could have appeared to influence the work reported in this paper.

## Acknowledgements

This research was sponsored by the US National Science Foundation (NSF) under grants CMMI-1662886 and CMMI-1662964. All opinions expressed in this paper are the authors' and do not necessarily reflect the policies and views of NSF.

## Appendix A. Code-based shear strength calculations

### A.1. List of Symbols

| | |
|---|---|
| $a$ | longitudinal on-center spacing of transverse stiffeners |
| $A_{fc}$ | cross-sectional area of compression flange |
| $A_{ft}$ | cross-sectional area of tension flange |
| $A_w$ | cross-sectional area of web |
| $b_f$ | width of flange (when tension and compression flanges are equivalent) |
| $b_p$ | smaller of the dimensions $a$ and $h$ (AISC 360–16) |
| $b_s$ | transverse width of stiffener |
| $E$ | modulus of elasticity |
| $F_{yf}$ | specified minimum yield stress of steel in the flanges |
| $F_{ys}$ | specified minimum yield stress of steel in the stiffeners |
| $F_{yw}$ | specified minimum yield stress of steel in the web |
| $h$ | clear distance between the flanges (i.e. height of web) |
| $I_{st}$ | moment of inertia of the transverse stiffeners about an axis in the web center for stiffener pairs |
| $I_{st1}$ | minimum moment of inertia of the transverse stiffeners required for development of the full shear post buckling resistance of the web panels (AISC 360–16) |
| $I_{st2}$ | minimum moment of inertia of the transverse stiffeners required for development of the web shear buckling resistance (AISC 360–16) |
| $M_{Ed}$ | applied bending moment (EC3, Part 1–5) |
| $M_{f,Rd}$ | moment resistance of the cross-section consisting of the effective area of the flanges only (EC3, Part 1–5) |
| $t_s$ | thickness of stiffener |
| $t_w$ | thickness of web |
| $V_{b,Rd}$ | design resistance for shear (EC3, Part 1–5) |
| $V_{bf,Rd}$ | contribution from the flange to the design resistance for shear (EC3, Part 1–5) |
| $V_{bw,Rd}$ | contribution from the web to the design resistance for shear (EC3, Part 1–5) |
| $V_n$ | nominal shear strength (AISC 360–16) |

### A.2. Per AISC 360–16, Chapter G: Shear Strength of Interior Web Panels

| | | |
|---|---|---|
| Calculate the web plate buckling coefficient, $\boldsymbol{k_v}$: | $k_v = 5 + \dfrac{5}{\left(\dfrac{a}{h}\right)^2}$ | (Eq. G2–5) |
| For a/h $\leq$ 3 Considering Tension Field Action: | | |
| Calculate web shear buckling coefficient[a], $\boldsymbol{C_{v2}}$: | For $\dfrac{h}{t_w} > 1.37\sqrt{k_v\dfrac{E}{F_{yw}}}$: | (Eq. G2–11) |
| Calculate nominal shear strength[a]: | For $\dfrac{2A_w}{A_{fc}+A_{ft}} \leq 2.5$ and $\dfrac{h}{b_f} \leq 6.0$: | (Eq. G2–7) |
| | $V_n = 0.6F_{yw}A_w\left(C_{v2} + \dfrac{1-C_{v2}}{1.15\sqrt{1+\left(\dfrac{a}{h}\right)^2}}\right)$ | |
| For a/b > 3 Without Tension Field Action: | | |
| Calculate web shear strength coefficient[a], $\boldsymbol{C_{v1}}$: | For $\dfrac{h}{t_w} > 1.10\sqrt{k_v\dfrac{E}{F_{yw}}}$: <br> $C_{v1} = \dfrac{1.10\sqrt{k_vE/F_{yw}}}{h/t_w}$ | (Eq. G2–4) |
| Calculate nominal shear strength: | $V_n = 0.6F_{yw}A_wC_{v1}$ | (Eq. G2–1) |
| Transverse Stiffeners Requirements: | | |
| Check the minimum stiffener dimension requirement[b]: | $\dfrac{b_s}{t_s} \leq 0.56\sqrt{\dfrac{E}{F_y}}$ | (Eq. G2–12) |
| Calculate minimum moment of inertia for stiffeners: | $I_{st1} = \left(\dfrac{h^4\rho_{st}^{1.3}}{40}\right)\left(\dfrac{F_{ys}}{E}\right)^{1.5}$ <br> where $\rho_{st} = 1.0$ (assuming that $F_{ys} = F_{yw}$) | (Eq. G2–14) |
| | $I_{st2} = \left(\dfrac{2.5}{\left(\dfrac{a}{h}\right)^2} - 2\right)b_pt_w^3 \geq 0.5b_pt_w^2$ | (Eq. G2–15) |
| Calculate stiffener moment of inertia: | $I_{st} = \dfrac{t_s(2b_s+t_w)^3}{12}$ | |
| Check stiffener moment of inertia[a]: | $I_{st} \geq I_{st2} + (I_{st1} - I_{st2})\rho_w$ <br> where $\rho_w = 1.0$ (i.e. required strength equals available strength for a test to failure) | (Eq. G2–13) |

### A.3. Per EC3, Part 1–5, Section 5: Shear Resistance of Interior Web Panels with Rigid Intermediate Stiffeners

| | | |
|---|---|---|
| Calculate elastic critical buckling strength, $\sigma_E$: | $\sigma_E = \dfrac{\pi^2 E t_w{}^2}{12(1-\nu^2)h^2}$ | (A.1.2) |
| Calculate steel strength adjustment factor, $\varepsilon$: | $\varepsilon = \sqrt{\dfrac{235}{F_{yw}\ (N/mm^2)}}$ | (5.1.2) |
| Calculate stiffener moment of inertia: | $I_{st} = \dfrac{t_s(2b_s+t_w)^3}{12}$ | |
| Check the following requirements for rigid intermediate stiffeners[a]: | If $\dfrac{a}{h} < \sqrt{2}$: $I_{st} > \dfrac{1.5h^3 t_w{}^3}{a^2}$<br>If $\dfrac{a}{h} \geq \sqrt{2}$: $I_{st} > 0.75h^3 t_w{}^3$ | (Eq. 9.6) |
| Calculate the shear buckling coefficient, $k_\tau$: | $k_\tau = 5.34 + 4.00\left(\dfrac{h}{a}\right)^2 + k_{\tau l}$ | (Eq. A.5) |
| | where $k_{\tau l} = 0$ (for no longitudinal stiffeners) | |
| Check the requirement for shear buckling consideration[a]: | $\dfrac{h}{t_w} > \dfrac{31}{\eta}\varepsilon\sqrt{k_\tau}$ | (5.1.2) |
| | where $\eta = 1.20$ (for steel grades up to and including S460) | |
| Calculate critical buckling strength, $\tau_{cr}$: | $\tau_{cr} = k_\tau \sigma_E$ | (Eq. 5.4) |
| Calculate modified slenderness, $\overline{\lambda}_w$: | $\overline{\lambda}_w = 0.76\sqrt{\dfrac{F_y}{\tau_{cr}}}$ | (Eq. 5.3) |
| Calculate the web contribution factor, $\chi_w$: | $\chi_w = \dfrac{1.37}{0.7+\overline{\lambda}_w}$ | (Table 5.1) |
| Calculate web contribution to shear buckling resistance: | $V_{bw,Rd} = \dfrac{\chi_w F_{yw} h t_w}{\gamma_{M1}\sqrt{3}}$ | (Eq. 5.2) |
| Calculate flange contributions to shear buckling resistance: | $V_{bf,Rd} = \left(\dfrac{b_f t_f{}^2 F_{yf}}{c\gamma_{M1}}\right)\left(1-\left(\dfrac{M_{Ed}}{M_{f,Rd}}\right)^2\right)$ | (Eq. 5.8) |
| | where $c = a\left(0.25 + \dfrac{1.6 b_f t_f{}^2 F_{yf}}{t_w h^2 F_{yw}}\right)$ | (5.4.1) |
| | where $\dfrac{M_{Ed}}{M_{f,Rd}} = 0.0$ (assuming pure shear[c]) | |
| | where $\gamma_{M1} = 1.0$ (for max. contribution[d]) | |
| Calculate design resistance for shear: | $V_{b,Rd} = V_{bw,Rd} + V_{bf,Rd}$ | (Eq. 5.1) |

### A.4. Notes

[a]Stiffeners in all prototype girder test sections with an applicable aspect ratio ($a/h$) met this condition.

[b]Stiffeners in the Hansen girder test sections met this condition while those for the Basler girders did not.

[c]Although the test section of each prototype girder does indeed have some bending moment per Fig. 4, the moment magnitude is very small relative to that of the shear. Assuming pure shear as a simplification will maximize the flange contribution to web shear buckling resistance.

[d]The value for partial factor $\gamma_{M1}$ is dependent on the application of the member under evaluation. For example, $\gamma_{M1} = 1.0$ for steel buildings (Eurocode 3, Part 1–1, Section 6.1, Note 2B [51]) and $\gamma_{M1} = 1.1$ for steel bridges (Eurocode 3, Part 2, Section 6.1, Note 2 [52]).

## References


[1] J.M. Wilson, On specifications for strength of Iron bridges, Trans. Am. Soc. Civ. Eng. 15 (1886) 389–414.
[2] AASHTO, AASHTO LRFD Bridge Design Specifications, 8th edition, American Association of State Highway and Transportation Officials, Washington, D.C., 2017. http://lrfdus8.digital.transportation.org.ezproxy.lib.lehigh.edu/LRFDUS8.aspx. (Accessed 14 July 2020).
[3] AISC, Specification For Structural Steel Buildings, American Institute of Steel Construction, Chicago, IL, 2016.
[4] CEN, EN 1993-1-5:2006 Eurocode 3: Design of Steel Structures - Part 1–5: Plated Structural Elements, European Committee for Standardization, Brussels, Belgium, 2009.
[5] D.W. White, M.G. Barker, Shear resistance of transversely stiffened steel I-girders, J. Struct. Eng. 134 (2008) 1425–1436, https://doi.org/10.1061/(ASCE)0733-9445(2008)134:9(1425).
[6] R.D. Ziemian (Ed.), Guide to Stability Design Criteria for Metal Structures, 6th Edition, 6th edition, John Wiley & Sons, Inc., Hoboken, NJ, USA, 2010. https://www.wiley.com/en-us/Guide+to+Stability+Design+Criteria+for+Metal+Structures%2C+6th+Edition-p-9780470085257 (accessed January 5, 2021).
[7] D.R. Hingnekar, A.Y. Vyavahare, Mechanics of shear resistance in steel plate girder: critical review, J. Struct. Eng. 146 (2020) 03120001, https://doi.org/10.1061/(ASCE)ST.1943-541X.0002484.
[8] C. Scandella, M. Neuenschwander, K.M. Mosalam, M. Knobloch, M. Fontana, Structural behavior of steel-plate girders in shear: experimental study and review of current design principles, J. Struct. Eng. 146 (2020) 04020243, https://doi.org/10.1061/(ASCE)ST.1943-541X.0002804.
[9] J.D. Glassman, M.E. Moreyra Garlock, A compression model for ultimate postbuckling shear strength, Thin-Walled Struct. 102 (2016) 258–272, https://doi.org/10.1016/j.tws.2016.01.016.
[10] H.T. Beach, A theory for spacing stiffeners in plate girders, Eng. News. 39 (1898) 322.
[11] H.T. Beach, Spacing stiffeners in plate girders, Eng. News. 41 (1899) 106.
[12] F.E. Turneaure, Tests of the stress in plate girder stiffeners, Eng. News. 40 (1898) 186.
[13] C.A.P. Turner, F.G. Shinner, Spacing stiffeners in plate girders, Eng. News. 40 (1898) 399.
[14] J.M. Wilson, Spacing stiffeners in plate girders, Eng. News. 40 (1898) 89.
[15] K. Basler, Strength of plate girders in shear, J. Struct. Div. 87 (1961) 151–180.
[16] K. Basler, B.T. Yen, J.A. Mueller, B. Thurlimann, Web Buckling Tests on Welded Plate Girders: Overall Introduction and Part 1: The Test Girders, Lehigh University, Bethlehem, PA, 1960.
[17] K. Basler, B.T. Yen, J.A. Mueller, B. Thurlimann, Web Buckling Tests on Welded Plate Girders Part 3: Tests on Plate Girders Subjected to Shear, Lehigh University, Bethlehem, PA, 1960.
[18] T. Hansen, Theory of Plasticity for Steel Structures: Solutions for Fillet Welds, Plate Girders and Thin Plates, Technical University of Denmark (DTU), 2006.
[19] T. Hansen, Post-buckling strength of plate girders subjected to shear - experimental verification, steel, Construction. 11 (2018) 65–72, https://doi.org/10.1002/stco.201710035.
[20] S.C. Lee, C.H. Yoo, Experimental study on ultimate shear strength of web panels, J. Struct. Eng. 125 (1999) 838–846, https://doi.org/10.1061/(ASCE)0733-9445(1999)125:8(838).
[21] S.C. Lee, C.H. Yoo, Strength of plate girder web panels under pure shear, J. Struct. Eng. 124 (1998) 184–194, https://doi.org/10.1061/(ASCE)0733-9445(1998)124:2(184).
[22] M.M. Alinia, M. Shakiba, H.R. Habashi, Shear failure characteristics of steel plate girders, Thin-Walled Struct. 47 (2009) 1498–1506, https://doi.org/10.1016/j.tws.2009.06.002.

[23] G.S. Stanway, J.C. Chapman, P.J. Dowling, Behaviour of a web plate in shear with an intermediate stiffener, Proceed. Instit. Civil Eng. Struct. Build. 99 (1993) 327–344, https://doi.org/10.1680/istbu.1993.24354.
[24] G.S. Stanway, J.C. Chapman, P.J. Dowling, A design model for intermediate web stiffeners, Proceed. Instit. Civil Eng. Struct. Build. 116 (1996) 54–68, https://doi.org/10.1680/istbu.1996.28154.
[25] S.C. Lee, C.H. Yoo, D.Y. Yoon, Behavior of intermediate transverse stiffeners attached on web panels, J. Struct. Eng. 128 (2002) 337–345, https://doi.org/10.1061/(ASCE)0733-9445(2002)128:3(337).
[26] M. Xie, J.C. Chapman, Design of web stiffeners: axial forces, J. Constr. Steel Res. 59 (2003) 1035–1056, https://doi.org/10.1016/S0143-974X(02)00115-3.
[27] Y.D. Kim, S.K. Jung, D.W. White, Transverse stiffener requirements in straight and horizontally curved steel I-girders, J. Bridg. Eng. 12 (2007) 174–183, https://doi.org/10.1061/(ASCE)1084-0702(2007)12:2(174).
[28] Y.D. Kim, D.W. White, Transverse stiffener requirements to develop shear-buckling and Postbuckling resistance of steel I-girders, J. Struct. Eng. 140 (2014) 04013098, https://doi.org/10.1061/(ASCE)ST.1943-541X.0000867.
[29] C.H. Yoo, S.C. Lee, Mechanics of web panel Postbuckling behavior in shear, J. Struct. Eng. 132 (2006) 1580–1589.
[30] M.E.M. Garlock, S.E. Quiel, P.Y. Wang, J. Alós-Moya, J.D. Glassman, Post-buckling mechanics of a square slender steel plate in pure shear, engineering journal-American Institute of Steel, Construction. 56 (2019) 27–46.
[31] K.C. Rockey, M. Skaloud, Influence of flange stiffness upon the load carrying capacity of webs in shear, in: IABSE 8th Congress, Final Report, International Association for Bridge and Structural Engineering, Zürich, Switzerland, 1968.
[32] K.C. Rockey, M. Skaloud, The ultimate load behaviour of plate girders loaded in shear, the, Struct. Eng. 50 (1972) 29–47.
[33] D.M. Porter, K.C. Rockey, H.R. Evans, The collapse behaviour of plate girders loaded in shear, the, Struct. Eng. 53 (1975) 313–325.
[34] T. Höglund, Shear buckling resistance of steel and aluminium plate girders, Thin-Walled Struct. 29 (1997) 13–30, https://doi.org/10.1016/S0263-8231(97)00012-8.
[35] S.C. Lee, D.S. Lee, C.H. Yoo, Further insights into Postbuckling of web panels. I: review of flange anchoring mechanism, J. Struct. Eng. 135 (2009) 3–10, https://doi.org/10.1061/(ASCE)0733-9445(2009)135:1(3).
[36] Y. Xiao, X.Y. Xue, F.F. Sun, G.Q. Li, Postbuckling shear capacity of high-strength steel plate girders, J. Constr. Steel Res. 150 (2018) 475–490, https://doi.org/10.1016/j.jcsr.2018.08.032.
[37] B. Johansson, M. Veljkovic, Steel plated structures, Prog. Struct. Eng. Mater. 3 (2001) 13–27, https://doi.org/10.1002/pse.59.
[38] Abaqus/Standard 2017, Dassault Systemes Simulia Corp., Johnston, RI, USA, 2017.
[39] P. Wang, K. Augustyn, A. Gomez, S. Quiel, M.E.M. Garlock, Influence of boundary conditions on the shear post-buckling behavior of thin web plates, in: Structural Stability Research Council Annual Stability Conference 2019, SSRC 2019, Structural Stability Research Council (SSRC), 2019, pp. 503–521. https://collaborate.princeton.edu/en/publications/influence-of-boundary-conditions-on-the-shear-post-buckling-behav. (Accessed 8 January 2021).
[40] P.Y. Wang, M.E.M. Garlock, T.P. Zoli, S.E. Quiel, Low-frequency sinusoids for enhanced shear buckling performance of thin plates, J. Constr. Steel Res. 177 (2021), 106475, https://doi.org/10.1016/j.jcsr.2020.106475.
[41] N. Mavrodontis, Converting engineering stress-strain to true stress-strain in Abaqus, Simuleon FEA Blog. October 9 (2017). https://info.simuleon.com/blog/converting-engineering-stress-strain-to-true-stress-strain-in-abaqus.
[42] S.C. Lee, J.S. Davidson, C.H. Yoo, Shear buckling coefficients of plate girder web panels, Comput. Struct. 59 (1996) 789–795, https://doi.org/10.1016/0045-7949(95)00325-8.
[43] A. Ghadami, V. Broujerdian, Shear behavior of steel plate girders considering variations in geometrical properties, J. Constr. Steel Res. 153 (2019) 567–577, https://doi.org/10.1016/j.jcsr.2018.11.009.
[44] Dassault Systemes Simulia Corp, Abaqus Analysis User's Guide. http://130.149.89.49:2080/v2016/books/usb/default.htm, 2015.
[45] E. Maiorana, C. Pellegrino, C. Modena, Imperfections in steel girder webs with and without perforations under patch loading, J. Constr. Steel Res. 65 (2009) 1121–1129, https://doi.org/10.1016/j.jcsr.2008.10.007.
[46] N. Liu, P. Plucinsky, A.E. Jeffers, Combining load-controlled and displacement-controlled algorithms to model thermal-mechanical snap-through instabilities in structures, J. Eng. Mech. 143 (2017) 04017051, https://doi.org/10.1061/(ASCE)EM.1943-7889.0001263.
[47] J.-H. Ahn, S. Kainuma, W.-H. Lee, Y.-J. Jeong, I.-T. Kim, Relationships between imperfections and shear buckling resistance in web plate with sectional damage caused by corrosion, Adv. Mater. Sci. Eng. 2016 (2016) 1–12, https://doi.org/10.1155/2016/6467589.
[48] P.Y. Wang, P.M. Masungi, M.E.M. Garlock, S.E. Quiel, Postbuckling mechanics in slender steel plates under pure shear: a focus on boundary conditions and load path, Thin-Walled Struct. 169 (2021), 108448, https://doi.org/10.1016/j.tws.2021.108448.
[49] K. Barth, Steel Bridge Design Handbook Design Example 1: Three-Span Continuous Straight Composite Steel I-Girder Bridge, Federal Highway Administration, Washington, D.C., 2015. https://www.fhwa.dot.gov/bridge/steel/pubs/hif16002/designexample01.pdf (accessed November 23, 2021).
[50] K. Barth, Steel Bridge Design Handbook Design Example 2A: Two-Span Continuous Straight Composite Steel I-Girder Bridge, Federal Highway Administration, Washington, D.C., 2015. https://www.fhwa.dot.gov/bridge/steel/pubs/hif16002/designexample02.pdf (accessed November 23, 2021).
[51] CEN, EN 1993-1-1:2005 Eurocode 3: Design of Steel Structures - Part 1–1: General Rules and Rules for Buildings, European Committee for Standardization, Brussels, Belgium, 2009.
[52] CEN, EN 1993-2:2006 Eurocode 3: Design of steel structures - Part 2: Steel Bridges, European Committee for Standardization, Brussels, Belgium, 2009. https://www.phd.eng.br/wp-content/uploads/2015/12/en.1993.2.2006.pdf. (Accessed 24 November 2021).